ACS Catalysis

Research Article

pubs.acs.org/acscatalysis

Crystal Plane Effect of Ceria on Supported Copper Oxide Cluster Catalyst for CO Oxidation: Importance of Metal−Support Interaction

Wei-Wei Wang,[†] Wen-Zhu Yu,[†] Pei-Pei Du,[‡] Hui Xu,[†] Zhao Jin,[†] Rui Si,[*,‡] Chao Ma,[*,§] Shuo Shi,[∥] Chun-Jiang Jia,[*,†] and Chun-Hua Yan[∥]

[†]Key Laboratory for Colloid and Interface Chemistry, Key Laboratory of Special Aggregated Materials, School of Chemistry and Chemical Engineering, Shandong University, Jinan 250100, People's Republic of China

[‡]Shanghai Synchrotron Radiation Facility, Shanghai Institute of Applied Physics, Chinese Academy of Sciences, Shanghai 201204, People's Republic of China

[§]Hefei National Laboratory for Physical Sciences at the Microscale, University of Science and Technology of China, Hefei, Anhui 230026, People's Republic of China

[∥]Beijing National Laboratory for Molecular Sciences, State Key Lab of Rare Earth Materials Chemistry and Applications, PKU-HKU Joint Lab in Rare Earth Materials and Bioinorganic Chemistry, Peking University, Beijing 100871, People's Republic of China

Supporting Information

ABSTRACT: Copper−ceria as one of the very active catalysts for oxidation reactions has been widely investigated in heterogeneous catalysis. In this work, copper oxide (1 wt % Cu loading) deposited on both ceria nanospheres with a {111}/{100}-terminated surface (**1CuCe-NS**) and with nanorod exposed {110}/{100} faces (**1CuCe-NR**) have been prepared for the investigation of crystal plane effects on CO oxidation. Various structural characterizations, especially including aberration-corrected scanning transmission electron microscopy (Cs-STEM), X-ray absorption fine structure (XAFS) technique, and in situ diffuse reflectance infrared Fourier transform spectroscopy (in situ DRIFTS), were used to precisely determine the structure and status of the catalysts. It is found that the copper oxides were formed as subnanometer clusters and were uniformly dispersed on the surface of the ceria support. The results from XAFS combined with the temperature-programmed reduction technique (H_2-TPR) reveal that more reducible CuO_x clusters with only Cu−O coordination structure exclusively dominated in the surface of **1CuCe-NS**, while the Cu species in **1CuCe-NR** existed in both CuO_x clusters and strongly interacting Cu-[O_x]-Ce. In situ DRIFTS results demonstrate that the CeO_2-{110} face induced a strongly bound Cu-[O_x]-Ce structure in **1CuCe-NR** which was adverse to the formation of reduced Cu(I) active sites, resulting in low reactivity in CO oxidation (r_{CO} = 1.8 × 10^{-6} mol_{CO} g_{cat}^{-1} s^{-1} at 118 °C); in contrast, CuO_x clusters on the CeO_2-{111} face were easily reduced to Cu(I) species when they were subjected to interaction with CO, which greatly enhanced the catalytic reactivity (r_{CO} = 5.7 × 10^{-6} mol_{CO} g_{cat}^{-1} s^{-1} at 104 °C). Thus, for copper−ceria catalyst, in comparison with the well-known reactive $\{110\}_{CeO2}$ plane, $\{111\}_{CeO2}$, the most inert plane, exhibits great superiority to induce more catalytically active sites of CuO_x clusters. The difference in strength of the interaction between copper oxides and different exposed faces of ceria is intrinsically relevant to the different redox and catalytic properties.

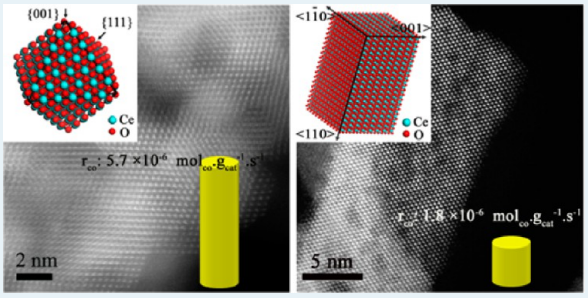

KEYWORDS: *copper−ceria catalyst, subnanometer clusters, crystal plane effect, metal−support interaction, redox properties*

1. INTRODUCTION

To date, research focused on the facet-dependent catalytic activities of metal and metallic oxide nanocatalysts has drawn growing interest, since it is known that the surface atomic arrangement is directly related to the catalytic reactivity. Therefore, shape-controlled synthesis of metal catalysts of Au,[1] Pt,[2] and Pd,[3] those that are bounded by low-/high-index faces have been extensively studied, in which the anisotropic nanocrystals act as a model catalyst system to investigate the surface sensitivity for a reaction.[4,5] In addition to well-shaped metal catalysts, metal oxide nanocrystals such as Co_3O_4-{110} nanorods,[6] TiO_2-{001} nanobelts,[7,8] Cu_2O-{111} octahedra/Cu_2O-{110} rhombic dodecahedra,[9] and CeO_2-{110} sheets[10]/CeO_2-{110}/{100}nanorods[11,12] have also been found to exhibit great superiority in catalytic performance in various reactions, due to the preferential exposure of reactive faces in the surfaces. These catalysts exposing certain reactive faces provide references for establishing practical model catalyst systems that are comparable to single-crystal catalysts for fundamental studies in heterogeneous catalysis. Up to now,

Received: November 14, 2016
Revised: January 4, 2017
Published: January 5, 2017

DOI: 10.1021/acscatal.6b03234
ACS Catal. 2017, 7, 1313−1329

studies on the crystal plane effect of solid catalysts have been more focused on pure metal or metal oxide systems; investigations of the synergic effects among different components on the basis of crystal plane effects in supported catalysts are still limited.

Among the various metal oxides as catalytic materials, ceria is used as either a catalyst or a catalyst support, a typical example of which is where the relationship between the exposed face and the catalytic reactivity has been explored in CO oxidation.[13−16] Theoretical calculations have revealed that CO had stronger chemisorption on the {110} and {100} faces of CeO_2 than on the {111} face,[13,14] which is consistent with the experimental results that the rodlike CeO_2 exposed {110}/{100} faces and cubelike CeO_2 with {100} plane showed obviously improved catalytic activities in CO oxidation in comparison to octahedron-like CeO_2 mainly exposing the {111} face.[15,16] The various nanoshapes of ceria with unique exposed surfaces have provided an ideal platform not only for an understanding of the crystal plane effects of pure ceria catalyst but also for an exploration of the role of the synergic effects among different components over the supported catalyst system. Currently, the support effects of CeO_2 for some catalytic reactions including Au/Pt/Pd supported on CeO_2 for CO oxidation,[17−19] Au/CeO_2 for water-gas shift reaction (WGS),[20] and Ru/CeO_2 for chlorobenzene combustion[21] have been investigated. It is unsurprising that metals supported on the reactive face CeO_2 supports that those with exposed {110} and {100} faces exhibit higher activity, while catalysts of metals supported on CeO_2-{111} (nanooctahedra) are relatively inactive. Therefore, this seems to draw the conclusion that reactive faces of the CeO_2 support induce correspondingly more active supported catalysts.

It is now generally acknowledged that CO oxidation in ceria-based catalysts is greatly enhanced, and numerous studies have investigated catalytically active species,[22] oxygen vacancies,[23,24] and metal−support interactions[25] for CO oxidation over ceria-based catalysts. Copper−ceria as a promising catalyst candidate for CO oxidation; in particular, it has been intensively investigated.[26−28] Since 1996, when Liu and Stephanopoulos proposed that Cu(I) species stabilized by the interaction between CuO and CeO_2 provide surface sites for CO chemisorptions,[26] much attention has been paid to CuO/CeO_2 catalysts in CO oxidation. Recently, by a combination of XANES and DRIFTS, Yao et al. further revealed the exclusive role of surface Cu(I) as the active site for the CO oxidation reaction over CuO/CeO_2 catalysts.[28] Theoretical simulations over CuO/CeO_2 catalysts exhibited that Cu atoms adsorbed at the surface of CeO_2-{111} prefer to exist as Cu(I),[29] whereas these atoms tend to be oxidized as Cu(II) on CeO_2-{110}.[30] In this case, for CuO_x/CeO_2 catalysts with different terminated surfaces of the CeO_2 support, the activity sequence should be reversed: the less active CeO_2-{111} face which could induce more Cu(I) sites is more catalytically active than CeO_2-{110}/{100} faces. However, current studies on the catalytic performance over various well-shaped CuO_x/CeO_2 catalysts for CO oxidation or PROX reactions have not been straightforward or even gave the conclusion that CeO_2-{110}/{100} induced activity obviously higher than that of CeO_2-{111}.[27,31,32] Therefore, we have a question as to what is the real crystal plane effect for copper−ceria catalyst for CO oxidation. Considering that copper species as active sites play a more crucial role in catalysis for CO oxidation, the crystal plane effect of the CeO_2 support is more intrinsically related to the metal−support interaction in CuO_x/CeO_2 catalyst so that different surface-terminated CeO_2 induces the formation of different copper species that determine the catalytic activity. Therefore, unlike pure metal or metal oxide catalysts, crystal plane effects in supported catalyst systems are complex. To get a better understanding of the relations among the exposed surface of CeO_2, the structure of copper species, and the resulting catalytic activity, a rationally designed CuO_x/CeO_2 catalyst system in which the interaction between copper oxide and ceria can be explored clearly needs to be established and investigated.

In this paper, we deposited subnanometer-sized CuO_x clusters onto CeO_2-{111}/{100} nanospheres and CeO_2-{110}/{100} nanorods as catalysts for CO oxidation. The very low loading of Cu (1 wt %) on ceria ensures the full interaction between CuO_x and CeO_2, which makes it possible to focus on the metal−support interaction originating from the crystal plane effect. Inconsistent with the current knowledge on the crystal plane effects of ceria-supported catalysts, CuO_x deposited on CeO_2-{111}/{100} nanospheres (NS) is much more reactive than that on CeO_2-{110}/{100} nanorods (NR) for CO oxidation. With the aid of Cs-corrected HRTEM/STEM, X-ray absorption fine structure adsorption (EXAFS), and in situ diffuse reflectance infrared Fourier transform spectroscopy (in situ DRIFTS), excluding the influence of the CeO_2-{100} face which exists both in NR and NS, we have demonstrated that the strongly bound Cu-[O_x]-Ce structure in the CeO_2-{110} face was adverse to the formation of Cu(I) species. In contrast, CuO_x clusters on the surface of CeO_2-{111} were easily reduced to Cu(I) species when they were subjected to interaction with CO. The stronger reduction trend of Cu(II) → Cu(I) in the CeO_2-{111} face is considered to be the intrinsic reason that ensures the high activity of the **CuCe-NS** catalysts. These results not only provide direct evidence for understanding the crystal plane effect that is relevant to the metal−support interaction and redox properties but also give guidance for the exploration of active sites on supported catalyst at the atomic level.

2. EXPERIMENTAL SECTION

2.1. Catalyst Preparation. All of the chemicals applied to our experiments are of analytical grade and were used without further purification or modification. Cerium nitrate ($Ce(NO_3)_3 \cdot 6H_2O$, 99.5%) and copper nitrate ($Cu(NO_3)_2 \cdot 3H_2O$, 98.0−102.0%) were purchased from Tianjin Kermal Chemical Reagent Factory. Sodium hydroxide (NaOH, ≥96.0%) and sodium carbonate (Na_2CO_3, 99.8%) were obtained from Sinopharm and Tianjin BoDi Chemical Reagent Factory, respectively. Acetic acid (CH_3COOH) and glycol ($HOCH_2CH_2OH$) were purchased from Tianjin Fuyu Fine Chemical Reagent Factory. Cetyltrimethylammonium bromide (CTAB, 99%) was obtained from Tianjin Guangfu Fine Chemical Research Institute.

The CeO_2 nanorods[12] (NR), CeO_2 nanoparticles[33] (NP), and CeO_2 nanospheres[34] (NS) were synthesized according to previous reports with minor alterations. Details of the syntheses of different CeO_2 supports are available in the Supporting Information. For the sequential DP synthesis, we refer to details given in our recent work.[35] The ceria powders (0.50 g) were suspended in 25 mL of Millipore water (18.25 MΩ) with stirring. Proper amounts of $Cu(NO_3)_2 \cdot 3H_2O$ were dissolved in 12.5 mL of Millipore water and added to the above suspension dropwise. During the whole process, the pH value of the

DOI: 10.1021/acscatal.6b03234
ACS Catal. 2017, 7, 1313−1329

solution was controlled at ca. 9 by adding Na_2CO_3 aqueous solution (0.50 M). The precipitates were further aged at room temperature for 1 h and then filtered and washed with Millipore water (1 L) at room temperature. The product was dried in air at 75 °C overnight and then calcined in still air at 400 °C for 4 h. In this work, the copper−ceria samples are denoted as ***x*CuCe-NR**, ***x*CuCe-NS**, and ***x*CuCe-NP** (x = 1, 5), where x is the copper content in weight percent ($x = [Cu/CeO_2]_{wt} \times 100\%$), NR, NS, and NP represent nanorods, nanospheres, and nanoparticles, respectively.

2.2. Characterization. The copper loadings were determined by inductively coupled plasma atomic emission spectroscopy (ICP-AES) on an IRIS Intrepid II XSP instrument (Thermo Electron Corp.). The nitrogen adsorption−desorption measurements were performed on a Builder SSA-4200 surface area analyzer at 77 K after activation of the samples at 200 °C for 6 h under vacuum. The BET specific surface area was calculated from the adsorption branch.

X-ray diffraction (XRD) was carried out on a PANalytical X'pert3 powder diffractometer (40 kV, 40 mA), using Cu Kα radiation (λ = 0.15406 nm). The powder catalyst after grinding was placed inside a quartz-glass sample holder before testing. Raman spectra were acquired by excitation of the sample at 473 nm using a Raman microscope system (Horiba Jobin Yvon) in the spectral window from 200 to 800 cm^{-1} with a spectral resolution of 2 cm^{-1}.

All of the investigated samples in transmission electron microscopy (TEM) characterization were sonicated in ethanol and then dropped on an ultrathin carbon film coated Mo grid. High-resolution TEM (HRTEM) images were carried out on a FEI Tecnai F20 microscope operating at 200 kV, and the aberration-corrected STEM images were obtained on a JEOL ARM200F microscope equipped with a probe-forming spherical-aberration corrector and Gatan image filter (Quantum 965).

X-ray photoelectron spectroscopy (XPS) analysis was performed on an Axis Ultra XPS spectrometer (Kratos, U.K.) with 225 W of Al Kα radiation. The C 1s line at 284.8 eV was used to calibrate the binding energies. The surface Ce^{3+} concentrations (Ce^{3+} atom %) were determined by integrating the areas of Ce 3d peaks with the CasaXPS software.

Temperature-programmed reduction by hydrogen (H_2-TPR) was carried out with a Builder PCSA-1000 instrument loaded with the sieved catalysts (20−40 mesh, 30 mg), with testing carried out from room temperature to 400 °C (5 °C min^{-1}) under a 5% H_2/Ar (30 mL min^{-1}) gas mixture. Before each measurement, the fresh samples were pretreated in pure O_2 at 300 °C for 30 min. The oxygen storage capacitys (OSCs)[12] of the samples were also measured with a Builder PCSA-1000 instrument under pluse mode. A 50 mg portion of the sample powder was pretreated from room temperature to 550 °C (5 °C min^{-1}) under a 5% H_2/Ar flow (30 mL min^{-1}), kept for 30 min, and flushed with pure He at 200 °C until the stability of the baseline; pure O_2 was pulsed into the reactor at 200 °C by several pulses at intervals of 1 min until the saturated adsorption of O_2. The volume of each pulse was 0.4 mL. The O_2-OSC values were determined by the amount of O_2 cumulative consumption during the O_2 pulses.

N_2O chemisorptions[36] were carried out to determine the Cu dispersion in a Builder PCSA-1000 instrument loaded with the sieved catalysts (20−40 mesh, 50 mg), which is composed of three sequential steps. Step 1, $CuO + H_2 \rightarrow Cu + H_2O$, represents the reduction of CuO. First, a flow of 5% H_2/Ar (30 mL min^{-1}) was used and tested from room temperature to 400 °C (10 °C min^{-1}). The amount of H_2 consumption (A_1) measured by TCD corresponds to the total amount of CuO. Step 2, $2Cu + N_2O \rightarrow Cu_2O + N_2$ represents the oxidation of surface Cu to Cu_2O by N_2O, which was used to evaluate the dispersion of copper catalysts. In this step, the reduced catalyst was cooled to 35 °C in He (30 mL min^{-1}) and was purging for 1 h. Then, pure N_2O (40 mL min^{-1}) was introduced to the catalyst at 35 °C for 1 h. Subsequently, the catalyst was purged with He (30 mL min^{-1}) for 0.5 h to remove the residual N_2O. Step 3, $Cu_2O + H_2 \rightarrow 2Cu + H_2O$, represents reduction of surface Cu_2O species. A flow of 5% H_2/Ar (30 mL min^{-1}) was also used and measurement was carried out from room temperature to 400 °C (10 °C min^{-1}). The amount of H_2 consumption (A_2) corresponds to the amount of Cu_2O. Then the dispersion (D) of CuO was calculated as $D = 2A_2/A_1 \times 100\%$.

The X-ray absorption fine structure (XAFS) spectra at the Cu K-edge (E_0 = 8979 eV) were obtained at the BL14W1 beamline of the Shanghai Synchrotron Radiation Facility (SSRF)[37] operated at 3.5 GeV in "top-up" mode with a constant current of 220 mA. The XAFS data were recorded in fluorescence mode with a standard Lytle ion chamber. The energy was calibrated according to the absorption edge of pure Cu foil. Athena and Artemis codes were used to extract the data and fit the profiles. For the X-ray absorption near edge structure (XANES) part, the experimental absorption coefficients as a function of energies $\mu(E)$ were processed by background subtraction and normalization procedures and reported as "normalized absorption". For the extended X-ray absorption fine structure (EXAFS) part, the Fourier transformed (FT) data in R space were analyzed by applying the first-shell approximation model for the Cu−O or Cu−Ce shell. The passive electron factors, S_0^2, were determined by fitting the experimental Cu foil data and fixing the Cu−Cu coordination number (CN) to be 12 and then fixing for further analysis of the measured samples. The parameters describing the electronic properties (e.g., correction to the photoelectron energy origin, E_0) and local structure environment including CN, bond distance (R), and Debye−Waller (DW) factor around the absorbing atoms were allowed to vary during the fitting process. The fitted range for k space was selected to be k = 3−12 $Å^{-1}$.

In situ diffuse reflectance infrared Fourier transform spectroscopy (in situ DRIFTS) characterization was carried out in a diffuse reflectance cell (Harrick system) equipped with CaF_2 windows on a Bruker Vertex 70 spectrometer using a mercury−cadmium−telluride (MCT) detector cooled with liquid nitrogen. In a typical steady test, the powder sample (ca. 40 mg) was pretreated in synthetic air (21 vol % O_2/79 vol % N_2) at 300 °C for 30 min and cooled to room temperature under pure N_2 (30 mL min^{-1}). Then a background spectrum was collected via 32 scans at 4 cm^{-1} resolution. The reaction gas with 1% CO/20% O_2/79% N_2 was introduced into the in situ chamber (30 mL min^{-1}) and heated in a stepped way (every 40 K); DRIFTS spectra were obtained by subtracting the background spectrum from subsequent spectra. The IR spectra for every step were recorded continuously for 40 min to reach the equilibrium. Analysis of the spectra has been carried out by using OPUS software.

For further investigation of the process of adsorption−desorption of CO over CuO_x/CeO_2 catalysts, a "CO-N_2−CO-O_2" test was measured with in situ DRIFTS. The process of

DOI: 10.1021/acscatal.6b03234
ACS Catal. 2017, 7, 1313−1329

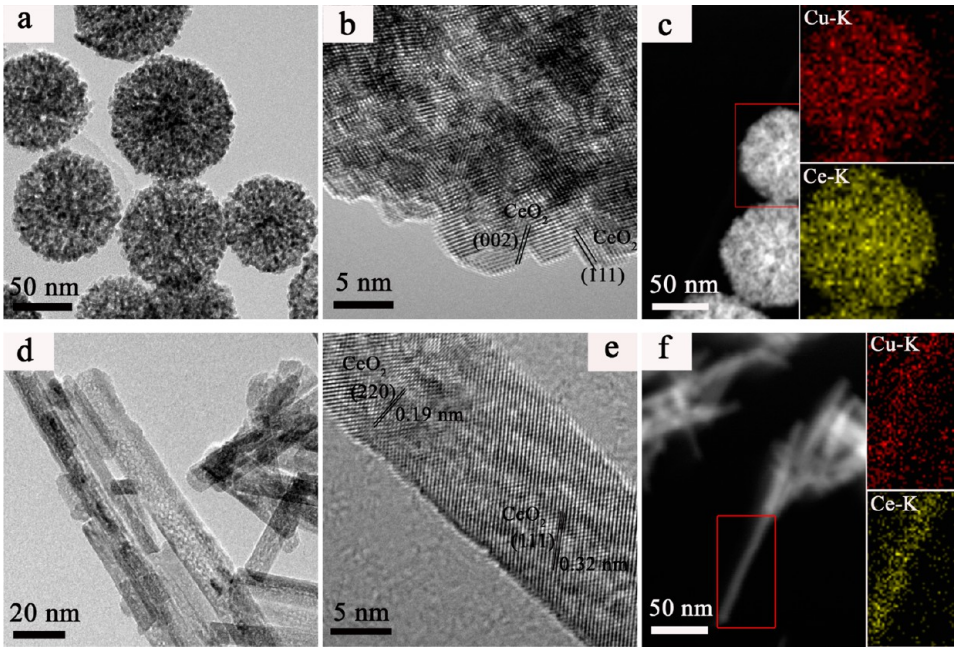

Figure 1. TEM (a, d) and HRTEM (b, e) images, together with STEM-EDS mapping results (c, f) for the **1CuCe** catalysts: (a–c) fresh **1CuCe-NS**; (d–f) fresh **1CuCe-NR**. Inserts show the corresponding STEM-EDS elemental mapping images, and the red boxes in the STEM images indicate the data collection areas.

Table 1. ICP-AES Analysis, BET Specific Surface Areas (S_{BET}), Oxygen Storage Capacity (OSC), H_2-TPR Reduction Temperatures (T_R) and H_2 Consumption (H_2), and XPS Analysis (O_{ad} and Ce^{3+} atom %) of the Chemical Compositions of 1CuCe Catalysts

catalyst	Cu (wt %)[a]	S_{BET} (m^2 g^{-1})	OSC (μmol g^{-1})[b]	T_R (°C)[c]	H_2 (μmol g^{-1})[d]	O_{ad} (%)[e]	Ce^{3+} (%)[e]
1CuCe-NR	1.2	92	349	190^{α}, 268^{β}	1162^{α}, 185^{β}	16^{α}, 22^{β}	17^{α}, 18^{β}
CeO_2-NR	–	106	202	–	–	–	–
1CuCe-NS	1.0	206	296	161, –	1075, 154	41, 31	22, 24
CeO_2-NS	–	219	171	–	–	–	–

[a]Determined by ICP-AES. [b]Measured by O_2 pulse. [c]Left, low-temperature reduction peak (α); right, high-temperature reduction peak (β). [d]Actual value of H_2 consumptions (α) and theoretical values of H_2 consumption calculated according to $Cu^{2+} \rightarrow Cu^0$ (β). [e]XPS of **1CuCe** catalysts before (α) and after (β) CO oxidation.

activation was carried out as described above. Then a background spectrum was collected at a certain temperature (80 or 120 °C) under pure N_2 (30 mL min^{-1}). The catalyst was exposed continuously to 2% CO in N_2 for CO adsorption for 30 min. Once CO gas was switched to an N_2 stream, also the corresponding IR spectra were recorded for 30 min. Then the catalyst was exposed to 2% CO in N_2 for CO readsorption for 30 min; ultimately 1% O_2 in an N_2 stream was introduced, in order to follow the surface changes during the CO removal process.

2.3. Catalytic Tests. CO oxidation activities of copper–ceria oxide catalysts were measured in a plug flow reactor using 50 mg of sieved (20–40 mesh) catalyst in a gas mixture of 1% CO/20% O_2/79% N_2 (from Deyang Gas Co., Jinan, 99.997% purity), at a flow rate of 67 mL min^{-1}, corresponding to a space velocity of 80000 mL h^{-1} g_{cat}^{-1}. Prior to the measurement, the catalysts were pretreated in synthetic air (21 vol % O_2/79 vol % N_2) at 300 °C for 30 min for activation. After that, the reactor was cooled to room temperature under a flow of pure N_2 gas. The catalytic tests were carried out in the reactant atmosphere by ramping the catalyst temperature (5 °C min^{-1}) from room temperature to 300 °C. The outlet gas compositions of CO and CO_2 were monitored online by nondispersive IR spectroscopy (Gasboard 3500, Wuhan Sifang Company, China).

The CO conversion was calculated according to the equation CO conversion = $CO_{reaction}/CO_{input}$.

3. RESULTS

3.1. Structure and Texture of Copper–Ceria Catalysts. The TEM images in Figure 1 show that the **1CuCe** samples keep their respective morphology of nanoshaped ceria supports. The **1CuCe-NS** sample has a spherelike shape with average sizes of around 130–150 nm (Figure 1a), which is comprised of much smaller particles with a crystallite size of 2–5 nm. Two surface terminating planes attributed to (002) and (111) were observed with respective interplanar spacings of 0.28 and 0.32 nm in the HRTEM image (Figure 1b), and there are clear voids among the small particles. Obviously, the predominantly exposed planes are {111} in **CeO_2-NS**, with a small amount of {100} planes. In combination with a previous study,[11] the structural models are shown in Figure 6c. The **1CuCe-NR** sample is composed of nanorods with lengths of 50–150 nm and a uniform width of ca. 10 nm (Figure 1d). The HRTEM image (Figure 1e and Figure S1b in the Supporting Information) displays the clear interplanar spacing of 0.28, 0.32, and 0.19 nm, corresponding to the (002), (111) and (220) lattice fringes of CeO_2. On the basis of the above images,

DOI: 10.1021/acscatal.6b03234
ACS Catal. 2017, 7, 1313–1329

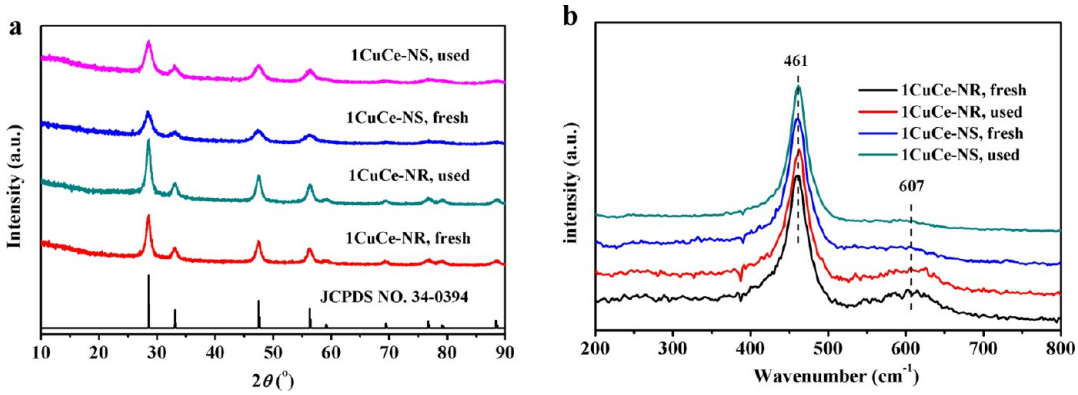

Figure 2. XRD patterns (a) and Raman spectra (b) of the as-prepared and used **1CuCe** catalysts.

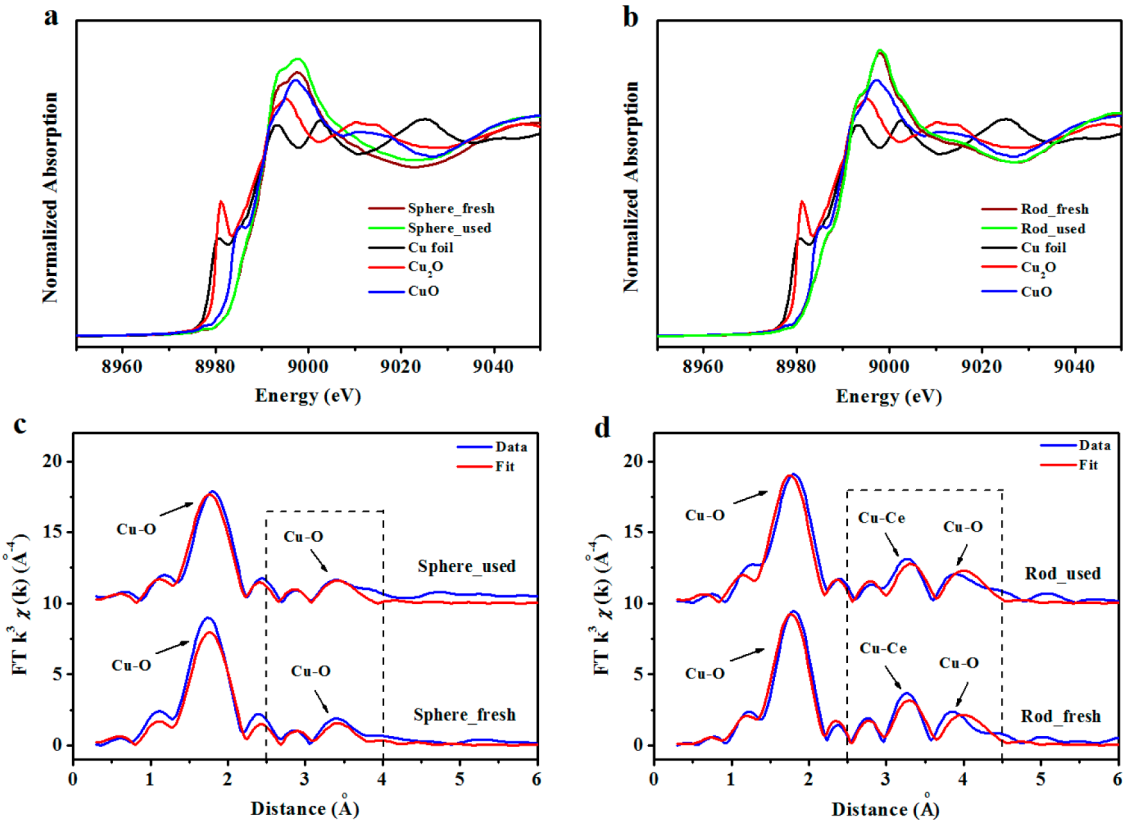

Figure 3. XANES (a, b) and EXAFS *R* space (c, d) spectra of **1CuCe** catalysts before and after CO oxidation: (a, c) **1CuCe-NS**; (b, d) **1CuCe-NR**.

the structural models of these nanorods are drawn in Figure 6f. Therefore, the above results show different exposed crystal planes: {111}- and {100}-dominated for NS and {110} and {100} for NR, which is similar to results given in previous reports.[12,34] No separated copper-containing phases (Cu/Cu_2O/CuO) were detected in HRTEM for the **1CuCe** catalysts (see Figure 1). The corresponding elemental mapping analysis (Figure 1c,f) conducted in the STEM-EDS mode confirms the homogeneous distribution of both Cu and Ce components in **1CuCe-NS** and **1CuCe-NR** catalysts.

The ICP-AES results (Table 1) show that the experimental Cu loadings of all catalysts are close to the target value. Diffraction patterns of fresh copper−ceria catalysts are illustrated in Figure 2a. The intense diffraction peaks of all catalysts can be attributed to the fluorite CeO_2 phase. In accordance with the related HRTEM results, no crystallized copper species are detected on copper−ceria catalysts in the **1CuCe** catalysts (Figure 2a). The possible reason is that the copper species are highly dispersed on the surface or the low copper loading is beyond the limitation of XRD detection. The broadening of the reflections ascribed to the **1CuCe-NS** with nanocrystalline nature, and the sharper reflections for **1CuCe-NR** implied their larger crystallite size in comparison with the **1CuCe-NS** catalysts. To finely determine the nanostructure of the **1CuCe** catalyst, Vis-Raman excited by a 473 nm laser was carried out (Figure 2b); it can be seen that the band at 460 cm^{-1} is ascribed to the F_{2g} vibration mode of the fluorite structure of CeO_2, and a broad band centered at ca. 600 cm^{-1} could be attributed to defect-induced (D) mode.[38] The relative intensity ratio $I(D)/I(F_{2g})$ in Table S1 in the Supporting Information, which could reflect the concentration of defects, clearly shows that **1CuCe-NR** contains more defect sites than

DOI: 10.1021/acscatal.6b03234
ACS Catal. 2017, 7, 1313−1329

Table 2. EXAFS Fitting Results (*R*, Distance; CN, Coordination Number) of 1CuCe Catalysts

sample	Cu−O		Cu−M[a]	
	R (Å)	CN	*R* (Å)	CN
Cu	—	—	2.558	12
Cu_2O	1.849	4	3.698	8
CuO	1.906	2	2.912	4
	1.985	2		
1CuCe-NR (fresh)	1.92 ± 0.01	4.0 ± 0.5	3.23 ± 0.04	2.8 ± 1.5
	4.25 ± 0.06	NF[b]		
1CuCe-NS (fresh)	1.93 ± 0.01	3.8 ± 0.4	—	—
	3.62 ± 0.08	NF[b]		
1CuCe-NR (used)	1.91 ± 0.01	4.0 ± 0.4	3.23 ± 0.05	2.3 ± 1.2
	4.25 ± 0.05	NF[b]		
1CuCe-NS (used)	1.93 ± 0.01	3.6 ± 0.4	—	—
	3.68 ± 0.07	NF[b]		

[a]Cu−Cu for Cu, Cu_2O, and CuO standards; Cu−Ce for the measured samples. [b]No reliable fitted values can be obtained for this CN.

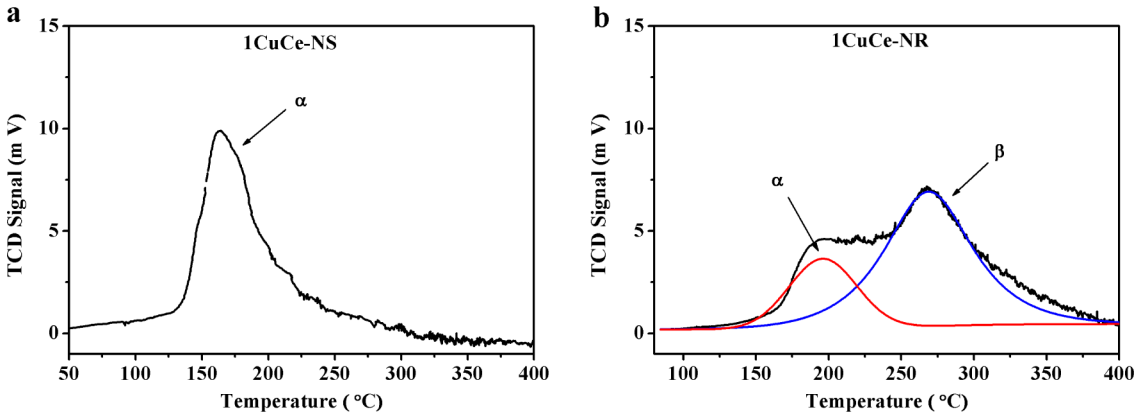

Figure 4. H_2-TPR profiles over **1CuCe** catalysts.

1CuCe-NS, whether before or after the CO oxidation reaction. Obviously, no separated CuO phase with Raman peaks located at 292 and 340 cm^{-1} was observed. Therefore, the XRD, Raman, and TEM results of **1CuCe** catalysts reveal that Cu species on ceria are highly dispersed and subnanometer sized. Nitrogen adsorption−desorption isotherms for **1CuCe** catalysts show that the **1CuCe-NS** composites exhibit the type H3 hysteresis loop that is characteristic of mesoporous materials. The surface areas are 206 and 92 m^2 g^{-1} for **1CuCe-NS** and **1CuCe-NR** catalysts, respectively, a slight decrease in comparison with the corresponding ceria support.

Since the X-ray diffraction technique is insensitive to low loadings of copper oxide clusters, to further verify the electronic and local coordination structure of the copper species on ceria, the XAFS technique was used over the as-prepared **1CuCe** catalysts. The XANES data for Cu K edge in Figure 3a,b clearly demonstrate the prevailing presence of Cu(II) in both nanosphere and nanorod samples, resulting in similar edge jumps from 8980 to 8990 eV. The XANES profiles in the range of 8990−9020 eV exhibit distinct line shapes between **1CuCe-NS** and **1CuCe-NR**, indicating their different coordinated structures. The EXAFS analysis for real-part *R* space (Figure S2 in the Supporting Information) displays that the structural phase in the range of 3.0−3.5 Å in **1CuCe-NR** is significantly different from that in **1CuCe-NS**. The phase, as well as the imaginary part, is also important during the EXAFS fit, but its contribution will be covered by the exhibition of magnitude *R* space. Therefore, the EXAFS fitting results were critical to distinguish the different metal−support interactions for **1CuCe-NR** and **1CuCe-NS** samples.

The related EXAFS spectra of Cu K edge (Figure 3c,d) exhibit a prominent peak at ca. 1.9 Å originating from the first shell of Cu−O contribution with a coordination number (CN) of around 4 for both **1CuCe-NS** and **1CuCe-NR** (see Table 2), which is quite consistent with the dominant Cu(II) species in each catalyst. Although the specific CN values cannot be obtained via the EXAFS fittings due to the much lower signal-to-noise level, Figure 3c,d clearly confirm the presence of other Cu−O shells at longer distances determined for nanospheres (3.6−3.7 Å) and nanorods (4.2−4.3 Å). Between the primary and secondary Cu−O shells, there is a Cu−Ce contribution at a distance of 3.2−3.3 Å with a CN of 2−3 for **1CuCe-NR** (Figure 3d and Table 2), corresponding to the creation of a Cu−O−Ce interaction, which is similar to the previous reports on Au−O−Ce[39] and Fe−O−Ce[40] systems. However, for **1CuCe-NS**, no such Cu−O−Ce structure can be detected by EXAFS, revealing its weaker metal−support interaction. As discussed above, we can draw a conclusion that both **1CuCe-NS** and **1CuCe-NR** catalysts contain ultrasmall CuO_x clusters composed of strong Cu−O coordination shells with (in **1CuCe-NR**) or without the Cu−O−Ce interaction (in **1CuCe-NS**). Thus, the specific copper structure in each catalyst can be determined as CuO_x clusters and Cu-[O_x]-Ce species for **1CuCe-NS** and **1CuCe-NR**, respectively.

In order to reveal the redox properties of copper species interacting with different exposed crystal planes of ceria, H_2-

DOI: 10.1021/acscatal.6b03234
ACS Catal. 2017, 7, 1313−1329

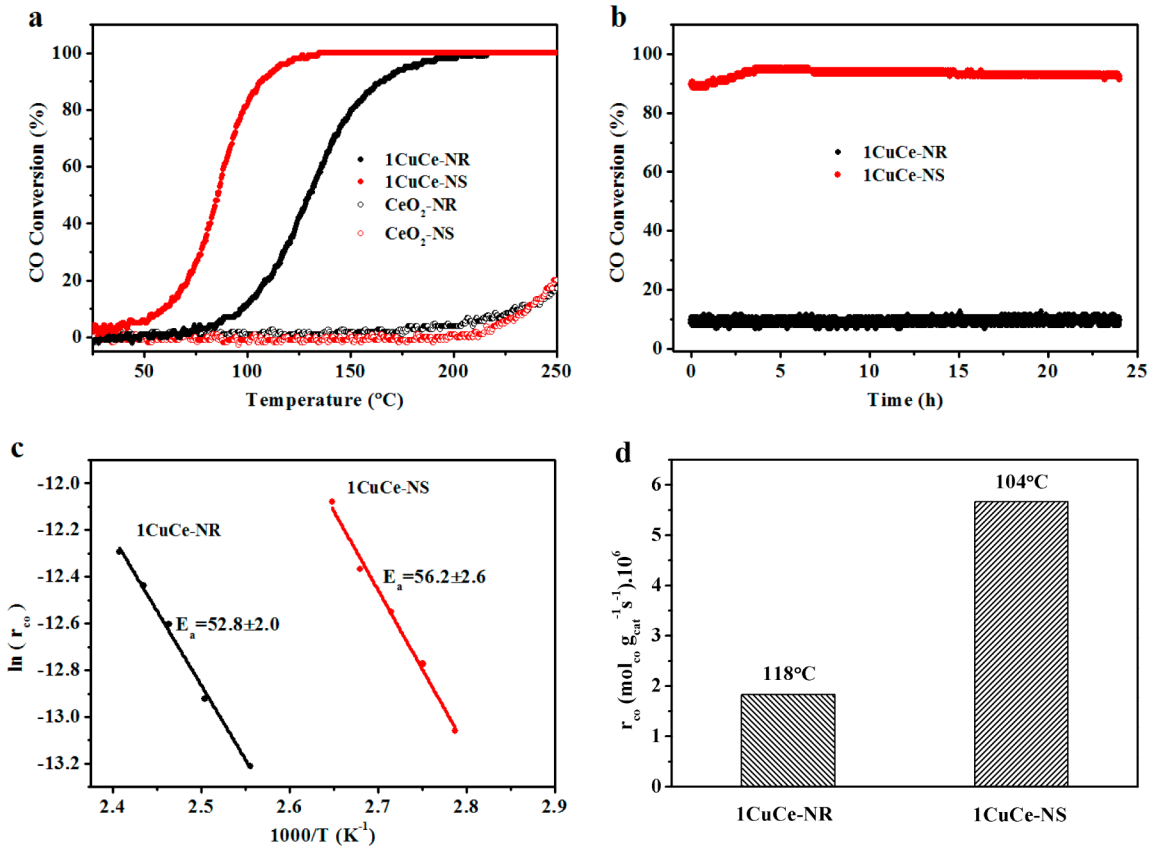

Figure 5. CO conversions over copper−ceria catalysts measured (a) under transient-state conditions and (b) at a constant temperature of 105 °C (1% CO/20% O_2/79% N_2, 80000 mL h^{-1} g_{cat}^{-1}). (c) Arrhenius plots of CO reaction rates under CO conversion between 5 and 15%. (d) CO reaction rates (r_{CO}) for **1CuCe** catalysts calculated from Arrhenius plots.

TPR was applied to the **1CuCe** catalysts. The **1CuCe-NR** catalyst shows two intense reduction peaks in Figure 4. However, only one reduction peak in the lower temperature region is observed for the **1CuCe-NS** catalyst. According to our recent work,[35] the peak at low temperature (α) is due to the reduction of CuO_x clusters by weak interaction with the CeO_2 and the reduction peak at high temperature (β) is attributed to the strong interaction of the Cu-[O_x]-Ce structure, which is quite consistent with the above EXAFS data corresponding to Cu−O and Cu−Ce bonding. The higher amount of hydrogen consumption for **1CuCe** catalysts in comparison with the theoretical value according to the complete reduction of $Cu^{2+} \rightarrow Cu^0$ (Table 1), as well as the shift in H_2-TPR profiles for **1CuCe** catalysts to lower temperature in comparison to the reduction of corresponding CeO_2 support, indicates that the deposition of copper oxide obviously facilitates the reduction of both copper oxide and ceria. In our recent study,[35] we determined two types of Cu species including a highly dispersed CuO_x cluster and Cu-[O_x]-Ce structure in the **5CuCe-NR** and **10CuCe-NR** system. We further identified that CuO_x clusters were the crucial active sites for the PROX reaction by comparing the status of copper oxide under oxidative and reductive pretreated conditions. However, in this work, the synergetic effect between copper oxide and CeO_2-{111}/{100} in **1CuCe-NS** could only render the CuO_x clusters by weak interaction with the ceria support and promote the reduction process, while the bimodal distribution of the CuO_x clusters and Cu-[O_x]-Ce structure and the more intense contribution (3.0−4.5 Å) in EXAFS spectra for **1CuCe-NR** are related to a lower dispersion degree of copper oxide adverse to the reduction process. The results above indicate the different structural states of copper species on ceria, and the metal−support interactions are obviously crystal plane dependent. However, neither the H_2-TPR nor EXAFS data can provide direct experimental evidence to justify the dispersion of copper oxide species in different catalysts.

3.2. Effects of Ceria Plane on the Catalytic Activities of Copper−Ceria Catalysts. The relationship between the catalytic activity and the structural/surface properties of the **1CuCe** catalysts was investigated by CO oxidation. The comparison of the reactivity of pure ceria supports of NR and NS presented in Figure 5a shows a similar result, with CO conversion below 5% up to 200 °C. However, the transient profiles of CO conversion reveal the much higher activity of the **1CuCe-NS**, in comparison to **1CuCe-NR** (T_{100} = 122 °C vs 194 °C). At a constant temperature of 105 °C (Figure 5b), the CO conversion during 24 h on stream is kept around 94% and 10% for **1CuCe-NS** and **1CuCe-NR**, respectively, which is quite consistent with the transient-state test. Apparent activation energy values determined from a kinetics study are ca. 53 and 56 kJ mol^{-1} for the **1CuCe-NR** and **1CuCe-NS** catalysts, respectively (Figure 5c), both of which are nearly in the range of 55−78 kJ mol^{-1} as previously reported,[41−43] indicating that they both have similar types of active sites and follow the same reaction pathway; however, this does not mean the same copper oxide species exist in **1CuCe-NR** and **NS**. As we have found in copper−ceria catalyst for the PROX reaction,[35] highly dispersed CuO_x clusters are identified as the active sites, while Cu-[O_x]-Ce species are catalytically inactive and contribute little to the activity in CO oxidation.

DOI: 10.1021/acscatal.6b03234
ACS Catal. 2017, 7, 1313−1329

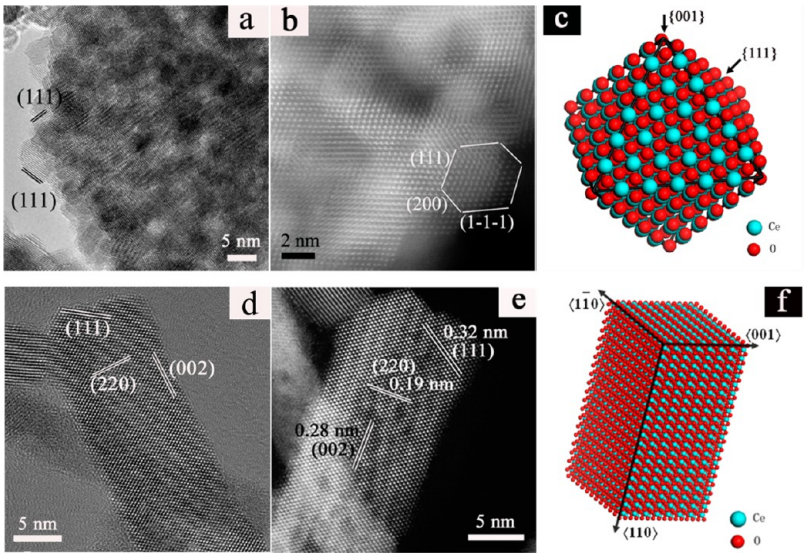

Figure 6. HRTEM (a, d) and HAADF-STEM (b, e) images of **1CuCe** catalysts after CO oxidation tests: (a, b) **1CuCe-NS**; (d, e) **1CuCe-NR**. Structure models of (c) **CeO_2-NS** and (f) **CeO_2-NR**.

The CO oxidation reaction rates for **1CuCe-NR** and **1CuCe-NS** are 1.8×10^{-6} mol_{co} g_{cat}^{-1} s^{-1} at 118 °C and 5.7×10^{-6} mol_{co} g_{cat}^{-1} s^{-1} at 104 °C, respectively (Figure 5d); the value is 3 times higher for **1CuCe-NS** than for **1CuCe-NR**, indicating that CeO_2-{111}/{100} is superior to CeO_2-{110}/{100} as a support for CuO_x. Such a support effect could be ascribed to the fact that CeO_2-{111} in NS in contact with CuO_x clusters facilitates the formation of Cu(I) during the redox process of Ce(IV)/Ce(III), thus enhancing the adsorption of CO to form Cu(I) carbonyl species.[44,45] However, another factor that should be taken into account is that CeO_2 serves as an oxygen supplier through either the formation of reactive oxygen species by oxygen gas reacting with oxygen vacancies on its surface or the direct involvement of lattice oxygen.[46,47]

In order to further compare the intrinsic activity of copper sites, we attempted to calculate the activity expressed per amount of active copper sites for the **1CuCe** catalysts. However, due to the low Cu loading in the catalysts, although N_2O chemisorption was employed to determine the Cu dispersion,[36] the *D* values were 130% for both **1CuCe-NR** and **1CuCe-NS**; these are greater than 100%, indicating that the influence of surface ceria cannot be excluded because of the strong interaction between copper and ceria and the presence of surface oxygen vacancies after the hydrogen pretreatment. Therefore, these values are not reliable or comparable for the determination of dispersion of copper oxide in the two catalysts via N_2O chemisorption. In addition, the structural variations between the two samples revealed from the H_2-TPR and XAFS results also suggested the different dispersions of the supported copper oxide in each catalyst.

It is necessary to consider the structural and/or textural changes after the CO oxidation test for the copper−ceria catalysts. The XRD patterns, Raman spectra (Figure 2b), and TEM images (Figure S1a,b,d,e in the Supporting Information) of the used copper−ceria catalysts reveal that no separated Cu-containing phase was generated; meanwhile, the corresponding elemental mapping results (Figure S1c,f) also confirm that the Cu and Ce elements were homogeneously distributed at the nanometer scale. Figure S1g shows that the edge of **CeO_2-NS** is composed of many specifically shaped particles; the predominant shape is truncated octahedral with exposed planes of {111} and a small amount of {001} planes. In order to further distinguish the copper species at the sub-nanometer-sized level, aberration-corrected STEM with sub-angstrom resolution was used to characterize the dispersion and configuration of the CuO_x clusters in the **1CuCe** catalysts after CO oxidation (Figure 6). However, due to the much higher atomic number (*Z*) of Ce in comparison with that of Cu, the contrast of Cu species in a very small size of only several atoms could not be distinguished from the thickness effect by CeO_2 in the HAADF-STEM mode. Only the crystalline lattice of CeO_2 was observed; thus, the copper clusters are very small at sub-nanometer size and are highly dispersed both on the **CeO_2-NR**-{110}/{100} surface and the **CeO_2-NS**-{111}/{100} surface. Furthermore, the XAFS technique was carried out to investigate the fine structure of copper oxide in **1CuCe** catalysts after CO oxidation. The XANES profiles (Figure 3a,b) and EXAFS fittings (Figure 3c,d and Table 2) verify almost the same oxidation state and local structure of copper between fresh and used samples for both **1CuCe-NS** and **1CuCe-NR** catalysts. These results demonstrated that the investigated copper−ceria catalysts were very stable during the CO oxidation reaction and consisted of highly dispersed CuO_x clusters for **1CuCe-NS** and mixed species of CuO_x clusters/strongly bound Cu-[O_x]-Ce structure for **1CuCe-NR** samples, respectively.

To further illuminate the surface composition of the **1CuCe** catalysts and the valence state of the elements and their relative abundance on the catalyst surface, XPS analysis was carried out. Figure 7a,b shows Cu 2p XPS spectra of the **1CuCe-NR** and **1CuCe-NS** catalysts before and after reaction. Although the low Cu loading results in poor signal to noise, which did not allow accurate confirmation of the quantitative relationship, the relative intensity of Cu 2p XPS spectra is somewhat higher in the **1CuCe-NR** sample in comparison to **1CuCe-NS**, further indicating a lower dispersion degree of copper in the former sample. The XPS peaks centered at 932.5 and 933.6 eV can be attributed to the Cu $2p_{3/2}$ region; 932.5 eV can be assigned to Cu(I)/Cu(0) species, and 933.6 eV corresponds to Cu(II) species. It can be seen that no contribution from Cu(I)/Cu(0) species is detected for the **1CuCe-NR** sample, while for

DOI: 10.1021/acscatal.6b03234
ACS Catal. 2017, 7, 1313−1329

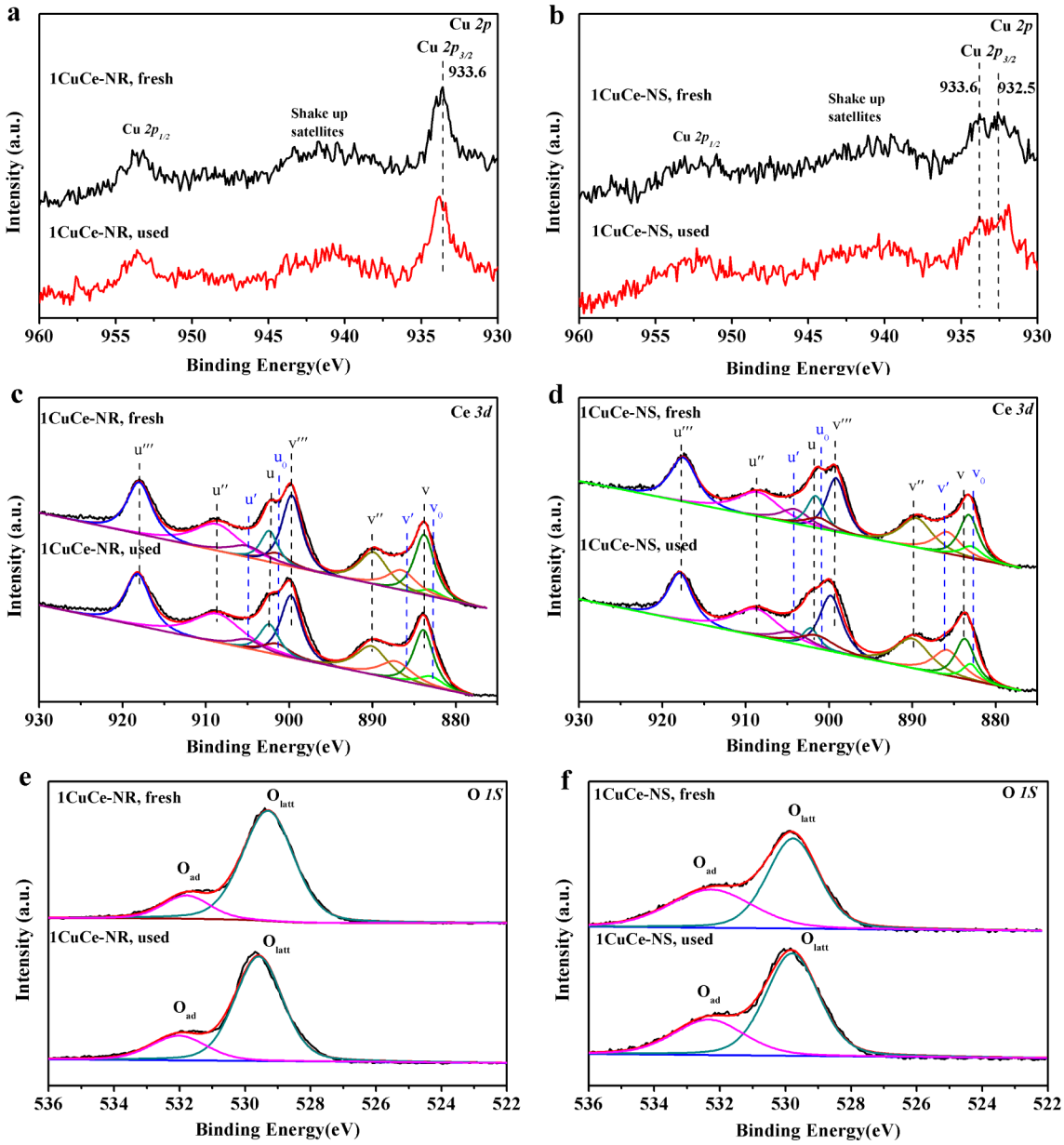

Figure 7. Cu 2p (a, b), Ce 3d (c, d), and O 1s (e, f) photoelectron profiles of fresh and used **1CuCe** catalysts: (a, c, e) **1CuCe-NR**; (b, d, f) **1CuCe-NS**.

1CuCe-NS the Cu(I)/Cu(0) species appeared before and after the reaction. A mixture of both Ce(IV) and Ce(III) oxidation states is detected for all the catalysts by analysis of the Ce 3d core-level XPS spectra (Figure 7c,d), which indicates the surfaces of the reduced catalysts accompanied by the formation of oxygen vacancies.[19,48] For **1CuCe-NS**, the abundance of Ce(III) (22%) is higher than that of **1CuCe-NR** (17%). Moreover, the reduction degree of the ceria surface is significantly increased for the sample after reaction (Table 1), indicating that the reduction of the state of the ceria surface over the catalyst results from the existence of a strong bond between copper and ceria.[33] Meanwhile, O 1s XPS spectra of the **1CuCe** catalysts also gave some information (Figure 7e,f). The presence of the main peaks at lower binding energy elucidates the existence of lattice oxygen (denoted as O_{latt}), and a shoulder peak at higher binding energy can be assigned to the adsorbed oxygen or oxygen in hydroxyl groups on the surface of the catalysts (denoted as O_{ad}),[19,21] while carbonate-type species could be ignored according to the following background spectra of in situ DRIFTS in Figure S3 in the Supporting Information. However, carbonate-type species may exist in the used **1CuCe** catalyst. Table 1 also gives the relative concentration of adsorbed oxygen ($O_{ad}/(O_{latt} + O_{ad})$). It is seen that **1CuCe-NS** (41%) had more surface oxygen species than **1CuCe-NR** (16%), which is in accord with the results obtained from the Ce 3d XPS spectra.

Furthermore, the oxygen storage capacity (OSC) of the CeO_2 support and **1CuCe** catalysts was also investigated (Table 1); we note that the OSC values for **CeO_2-NR** and **NS** are comparable (202 vs 171 umol g^{-1}). In comparison with the CeO_2 supports, **1CuCe** catalysts have higher OSC values due to the addition of CuO_x. The **1CuCe-NS** sample exhibited an OSC value of 296 umol g^{-1}, which is lower than that of **1CuCe-NR** (349 umol g^{-1}) despite the surface area of the former (206

DOI: 10.1021/acscatal.6b03234
ACS Catal. 2017, 7, 1313−1329

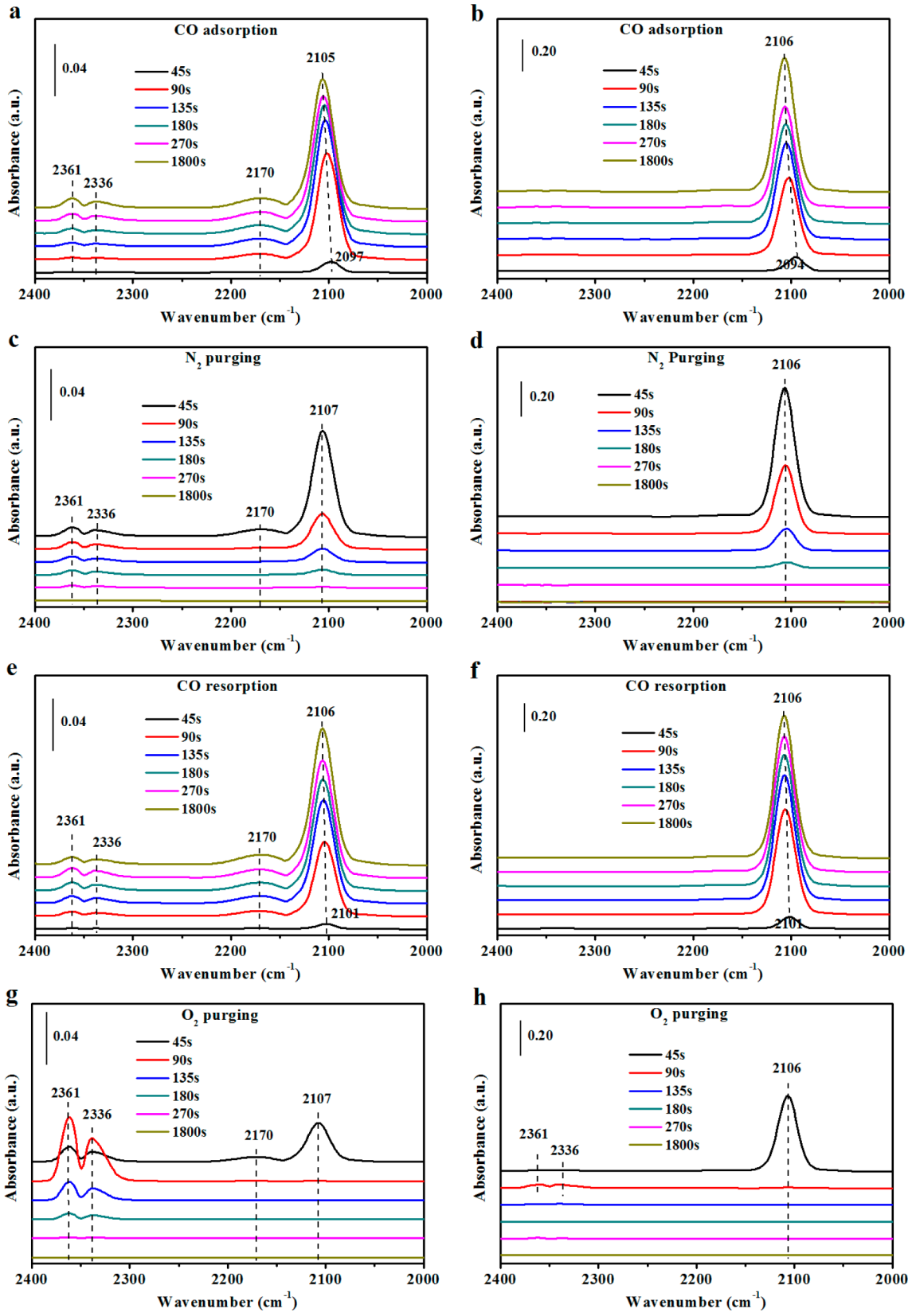

Figure 8. In situ DRIFTS study of (a, b) CO adsorption, (c, d) N_2 purging, (e, f) CO readsorption, and (g, h) O_2 removal on (a, c, e, g) **1CuCe-NR** and (b, d, f, h) **1CuCe-NS**. The catalysts were pretreated in situ at 300 °C under air flow in the DRIFTS reaction cell before data collection (CO flow rate, 30 mL min^{-1}; catalyst mass, 40 mg; temperature, 120 °C).

$m^2\ g^{-1}$) being 2 times higher than that of the latter (92 $m^2\ g^{-1}$). The obtained OSC value is in accord with the Raman result. Therefore, on the basis of the above H_2-TPR, OSC and Raman results, we suggest that the much higher CO conversion activity

DOI: 10.1021/acscatal.6b03234
ACS Catal. 2017, 7, 1313−1329

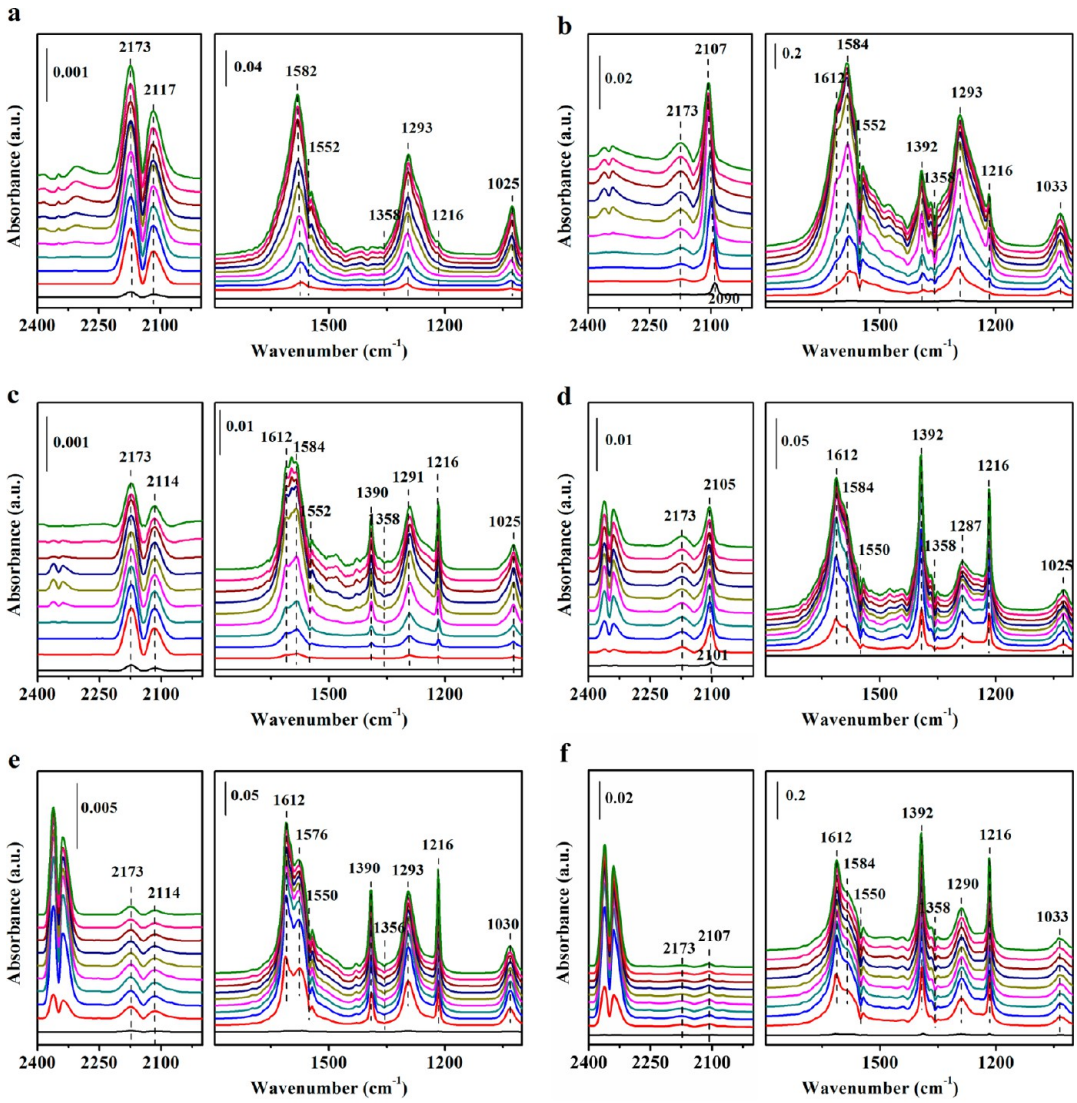

Figure 9. In situ DRIFTS taken for 40 min (from bottom to top: 1, 2, 3, 4, 6, 10, 15, 30, 35, and 40 min) under the reaction conditions (1% CO/20% O_2/N_2 flow) at (a, b) 40 °C, (c, d) 80 °C, and (e, f) 120 °C for (a, c, e) **1CuCe-NR** and (b, d, f) **1CuCe-NS**.

for **1CuCe-NS** with the {111}/{100} sample results from the existence of Ce(III) promoting the reduction of Cu(II) for **1CuCe-NS**, which is consistent with the theoretical simulation results that Cu adsorbed at the surface of the stoichiometric CeO_2-{111} face is Cu(I).[29] Thus, the different synergetic interactions between CuO_x and CeO_2-{110}/{100} and CeO_2-{111}/{100} leading to different reduction properties are the main factors that determine catalysis for CO oxidation.

On the basis of the XANES results in Figure 3, the only signal for Cu(II) species is observed for **1CuCe** catalysts. However, XPS data show that the Cu(II) species exclusively dominates in the **1CuCe-NR** sample while a low concentration of Cu(I)/Cu(0) species is observed in **1CuCe-NS**. Thus, to gain further insight into the redox properties of the catalysts, in situ DRIFTS was also used to detect the onset of Cu(II) → Cu(I) during the CO adsorption on the surfaces of **1CuCe-NR** and **1CuCe-NS** catalysts in a "CO-N_2−CO-O_2" mode at 120 °C. Both samples display bands in the 2000−2400 cm^{-1} zone corresponding to $Cu^{\delta+}$-CO species and gaseous CO_2 under CO adsorption. For the $Cu^{\delta+}$-CO system, spectral ranges of 2200−2140 and 2100−2000 cm^{-1} are typical for CO adsorption on Cu^{2+} and Cu^0 sites,[49] respectively. The diverse signals reveal a spontaneous variation in the extent of reduction of CuO_x/CeO_2 evolved following extended exposure. For **1CuCe-NR** (Figure 8a), the IR band at 2105 cm^{-1}, attributed to linear CO adsorbed on Cu^+ sites (Cu^+-CO),[50] increased rapidly and reached saturation adsorption at 180 s. An apparent band at ca. 2170 cm^{-1} attributed to gaseous CO was accompanied by Cu^+-CO species. The bands at 2336 and 2361 cm^{-1} for gaseous CO_2 appear at 90 s, suggesting that the incoming CO reduces the surface oxide species.[33] With regard to **1CuCe-NS** (Figure 8b), Cu^+-CO species at 2106 cm^{-1} increased gradually and continued to adsorb up to 1800 s, indicating more Cu(I) species in the **1CuCe-NS** sample. The magnified inset in Figure S4a in the Supporting Information shows a weak low-frequency peak at 2060 cm^{-1}, which could be related to Cu^0-carbonyl (Cu^0-CO)[49] considering that 2% CO/N_2 gas provides a reducing atmosphere. The signals of gaseous CO and CO_2 are hardly observed in the IR spectra of the **1CuCe-NS** sample due to the strong adsorption of Cu^+-CO, which is 10 times stronger in intensity than that in the **1CuCe-NR** sample. It is noted that the frequency signal (2097 or 2094 cm^{-1}) is the first

DOI: 10.1021/acscatal.6b03234
ACS Catal. 2017, 7, 1313−1329

to appear for both **1CuCe-NR** and **1CuCe-NS** catalysts, which may result from the displacement of weakly adsorbed oxygen species at intrinsic Cu^+ defects at the surface.[51] The apparent blue shift of the carbonyl peak, reaching a steady position quickly around 135 s, is likely due to strong reduction of the remaining Cu(II) component under 2% CO/N_2.[52] During the N_2-purging process, the carbonyl peak gradually decayed and absolutely disappeared at around 270 s for both **1CuCe-NR** and **1CuCe-NS** catalysts (Figure 8c,d). The subsequent process corresponding to CO readsorption (Figure 8e,f) still reveals the much higher intensity of the Cu^+-CO peak for the **1CuCe-NS** sample, in comparison to **1CuCe-NR**, which is similar to the first adsorption process. Once the CO adsorption lasts 30 min, the gas channel was switched immediately to 1% O_2/N_2; the correspondingly collected spectra are shown in Figure 8g,h. The Cu^+-CO peak vanished already upon initial contact with the 1% O_2/N_2 after 45 s accompanied by the appearance of CO_2 for **1CuCe-NR** and **1CuCe-NS** catalysts, verifying that the respective intensities of these Cu^+-CO species are related to the amount of active sites available for oxygen to contact.

As demonstrated by H_2-TPR, EXAFS, and in situ DRIFTS CO adsorption results, CeO_2-{111}/{100} in **1CuCe-NS** causes a stronger synergic interaction between copper and ceria and facilitates the reduction of Cu(II) → Cu(I). However, the Cu-[O_x]-Ce structure induced by CeO_2-{110}/{100} seems adverse to the reduction process. In combination with the Raman results, we infer that the greater the number of defect sites in **1CuCe-NR** samples, the stronger the interaction established between copper and ceria, which induced the difficulties in the reduction of copper oxide and the weak Cu^+-CO absorption. Therefore, the much higher activity of CO oxidation for **1CuCe-NS** in comparison to that of **1CuCe-NR** indicates that, in comparison with the defect site, the copper species should play a more prominent role in this copper−ceria system.

CO and O_2 coadsorption monitoring by in situ DRIFTS was further conducted under steady-state conditions during CO oxidation. The background spectrum before introduction of CO gas was collected to examine possible differences between the two catalysts in terms of amount or type of hydroxyls or carbonate-type species present in each case (Figure S3 in the Supporting Information). No apparent difference is detected in the spectra for the initial samples. Figure 9 and Figure S5 in the Supporting Information display the time evolution of three distinct spectral zones on contact with the reactant mixture for 40 min in the reaction gas (1% CO, 20% O_2, balanced with N_2) at the indicated temperature. The first zone at higher wavenumbers of 2800−4000 cm^{-1} (Figure S5) displays bands corresponding mainly to hydroxyl species. According to previous analyses of ceria-related materials, the relatively narrow bands at ca. 3712−3690 cm^{-1} can be attributed to isolated hydroxyls (monocoordinated to surface cerium cations),[53] the band at ca. 3618 cm^{-1} is due to an OH stretching vibration which formed upon interaction of CO (or CO_2) with monodentate hydroxyls,[53] and a broad band extending from ca. 3500 to 3000 cm^{-1} belongs to associated species. Peaks assigned to hydroxyl species for the **1CuCe-NS** sample are stronger than those of **1CuCe-NR** during the test, and the intensity of the OH stretching vibration at ca. 3618 cm^{-1} increases with the appearance of bicarbonate species. The second zone at lower wavenumbers below 1800 cm^{-1} displays bands corresponding mainly to carbonate or related species, basically chemisorbed on ceria.[53,54] Usually, three major carbonate species form for copper−ceria catalysts. Here, a carbonate bidentate species (bands at 1565, 1298, and 1014 cm^{-1}),[55] a bicarbonate species (bands at ∼1393 and 1217 cm^{-1} with a shoulder at 1611 cm^{-1}),[55] and formate species (negative signals at 1552 and 1358 cm^{-1} found at 1550 and 1358 cm^{-1})[52] have been detected over **1CuCe-NR** and **1CuCe-NS** catalysts. Among the above species, the most intense peaks in this zone can be ascribed to the carbonate bidentate and bicarbonate species (Figure 9a−d); moreover, the bicarbonate species is predominant on heating above 80 °C both for **1CuCe-NR** and **1CuCe-NS** catalysts (Figure 9e,f). According to previous reports, bicarbonate and formate species might be the inactive species formed during the catalytic process and bidentate carbonates are suggested to be the initial species for CO adsorption on CeO_2:Ln dopant series.[56] A recent report has provided experimental evidence that bicarbonates favored faster CO oxidation rates in comparison to carbonates for a CuO/CeO_2 catalyst.[57] These various carbonates seemed to be involved in the transfer and desorption of CO_2 as the products, although they play different roles in the reaction. However, in this work, we did not find any measurable deactivation on **1CuCe-NR** or **-NS** samples (Figure 5b). Thus, we cannot claim that the surface carbonates intervene in the CO oxidation. It can be noted that there are some differences between **1CuCe-NR** and **1CuCe-NS** catalysts in DRIFT spectra. (1) Peaks assigned to carbonate or related species for the **1CuCe-NS** sample are quite stronger than those of **1CuCe-NR** during the test. The results show that carbonate species are more easily formed on CeO_2-{111}/{100} than on CeO_2-{110}/{100}. (2) Bicarbonate species can be obviously detected at 1612, 1392, and 1216 cm^{-1} for the **1CuCe-NS** sample at 40 °C, while the prevailing presence of carbonates species is noted for **1CuCe-NR**. The presence of surface bicarbonates, which have lower thermal stability in comparison to carbonate species, would favor a faster desorption of CO_2, leaving the surface available for further chemisorptions, through which the CO oxidation is accelerated.[57]

In order to further examine the reaction pathway of CO adsorption/oxidation and the valence states of copper species, a third spectral zone from 2400 to 2000 cm^{-1} was also collected. This shows that, in addition to the bands centered at 2360 and 2341 cm^{-1} corresponding to gaseous CO_2, bands at ca. 2173 and 2119 cm^{-1} attributed to gaseous CO and the band at ca. 2073−2117 cm^{-1} for the $Cu^{\delta+}$-CO system are also detected at the indicated temperature. A spectral range of 2200−2140 cm^{-1} is typical for CO adsorption on Cu^{2+} sites (Cu^{2+}-CO),[50] which can be disregarded for our system. The results of repeated experiments in Figure 9f also verify the existence of the low-frequency feature at ca. 2073 cm^{-1}. However, the peak at ca. 2073 cm^{-1} (Figure S4b in the Supporting Information) attributed to the Cu^0-carbonyl peak (Cu^0-CO)[49] could be eliminated considering the poor signal to noise and the weak adsorption of carbonyl at O_2/CO = 20, which is 1% less in intensity than that in the CO-adsorption experiment (Figure 8b). The medium-frequency peak at ca. 2090−2115 cm^{-1} belongs to the Cu^+ carbonyl peak (Cu^+-CO),[50] in which carbonyls formed on Cu^+ on the surface of the CeO_2 support. In Figure 9a, the weak Cu^+-CO species (ca. 2117 cm^{-1})[58,59] in the **1CuCe-NR** sample overlapped with the gaseous CO signal at 40 °C. The band at 2090 cm^{-1} is the first to appear in Figure 9b for the **1CuCe-NS** sample. It may result from the displacement of weakly adsorbed oxygen species at intrinsic Cu^+ defects at the surface.[51] The subsequent apparent blue shift

DOI: 10.1021/acscatal.6b03234
ACS Catal. 2017, 7, 1313−1329

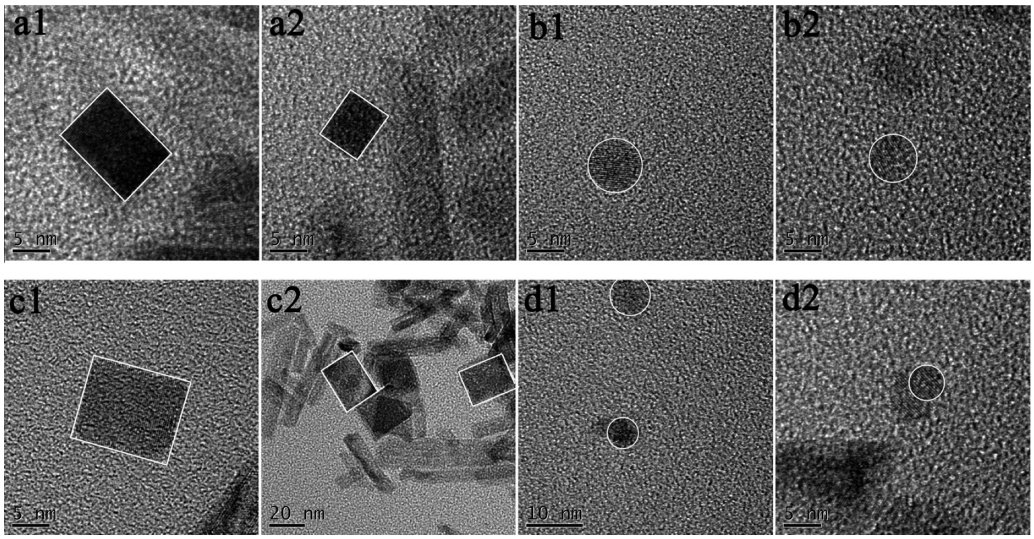

Figure 10. HRTEM images of the cross-sectional samples for **CeO_2-NR** and **1CuCe-NR** samples: (a) uncalcined **CeO_2-NR**; (b) calcined **CeO_2-NR**; (c) **1CuCe-NR U-C**; (d) **1CuCe-NR C-C**.

of the carbonyl peak at 2090 cm^{-1} gradually shifts to 2107 cm^{-1}, reaching a steady intensity and position around 15 min, which is likely due to spontaneous reduction of a fraction of the remaining Cu(II) component. As discussed above, the **1CuCe-NS** sample, containing more Ce^{3+}, has a greater ability to assist the redox equilibrium Cu(II) + Ce(III) ↔ Cu(I) + Ce(IV) in shifting to the right to form more Cu(I) species, which is difficult in **1CuCe-NR**. Cu^+-CO giving rise to bands at ca. 2117 and 2107 cm^{-1} for **1CuCe-NR** and **1CuCe-NS** catalysts, respectively, decreased in concentration with increasing temperature up to 120 °C and practically disappeared above that temperature, most likely due to thermal stability effects and the production of CO_2 rather than being a result of catalyst reduction or reconstruction.[60] It is worth noting that the intensity of Cu^+-CO bands appears to be higher for **1CuCe-NS** than for the **1CuCe-NR** sample; on consideration of the activity (Figure 5a), it is suggested that the CO oxidation is proportional to the intensity of the Cu^+-CO band. For the **1CuCe-NR** sample, CO_2 is not detected up to 80 °C, while CO_2 appears at around 15 min accompanied by the steady presence of Cu^+-CO at 40 °C for **1CuCe-NS**. This means that Cu^+ remains stable in **1CuCe-NS** sample, while little Cu^+-CO could exist in **1CuCe-NR**. The intensities of CO_2 elevated gradually with an increase in temperature from 40 to 120 °C, with the intensities of Cu^+-CO decreasing simultaneously.

On the basis of all the above results, we can roughly conclude that the CuO_x clusters in both **1CuCe-NS** and **1CuCe-NR** catalysts are the active sites for the CO oxidation; however, the Cu-[O_x]-Ce species in **1CuCe-NR** seems adverse to the reactivity. Then we attempted to quantify the amount of Cu-[O_x]-Ce species and CuO_x clusters on the basis of the H_2-TPR results. The TOF for the **1CuCe-NR** and **1CuCe-NS** samples is calculated only on the basis of the amount of CuO_x species because we have identified the CuO_x clusters, not the Cu-[O_x]-Ce species, as the active sites. As can be seen in Figure 4, it appears that all the copper species are formed as CuO_x clusters (corresponding to the α peak) in the **1CuCe-NS** sample; meanwhile, both CuO_x clusters and Cu-[O_x]-Ce species (corresponding to the β peak) are present in the **1CuCe-NR** sample. Since the aberration-corrected HAADF-STEM results (Figure 6) have verified that no copper oxide particles (>1 nm) were found in our system, we can confirm that the copper oxide species were formed as very small clusters (<1 nm) or single atoms. Therefore, we suppose the full dispersion of active copper (D = 100%) for the **1CuCe-NS** sample, while the dispersion of active copper for the **1CuCe-NR** sample was denoted as $D = S(\alpha)_{NR}/S(\alpha)_{NS}$ = 31%. The obtained TOFs for **1CuCe-NR** and **1CuCe-NS** are 4.2×10^{-2} s^{-1} at 118 °C and 4.8×10^{-2} s^{-1} at 104 °C, respectively, both of which are very close to each other. Considering the nearly identical apparent activation energy values determined from a kinetics study (Figure 5c) which indicate the same reaction pathway, the almost identical TOF values further confirm that the CuO_x clusters that interact weakly with the ceria support are the actual active sites for CO oxidation.

3.3. Verification of Crystal Plane Effects over Copper–Ceria Catalysts. *3.3.1. Exclusion of the Influence of Surface Area of Catalyst on CO Oxidation Activity.* To further verify the effects of CeO_2-{111}/{100} on the CO oxidation activity and eliminate the difference in specific surface areas for **1CuCe-NS** and **1CuCe-NR** catalysts, in which the former is about twice as high as that in the latter sample, which may favor a better dispersion of copper oxide on the **CeO_2-NS** surface, a wormhole-like mesostructured CeO_2-{111}/{100} nanoparticles (**1CuCe-NP**, seen in Figure S6a,b in the Supporting Information) sample with surface area (123 m^2 g^{-1}) comparable to that of **1CuCe-NR** (92 m^2 g^{-1}) was investigated. It is found that the **1CuCe-NP** sample exhibits activity similar to that of **1CuCe-NS** (Figure S7 in the Supporting Information) and is much more active than **1CuCe-NR**. The H_2-TPR results in Figure S6c show a main reduction peak in the 100–200 °C range, which is consistent with the **1CuCe-NS** sample. The related EXAFS spectra (Figure S8 and Table S2 in the Supporting Information) indicate a prominent peak at ca. 1.9 Å from the contribution of the first shell of Cu–O and an unchanged coordination number (3–4) before and after the reaction. Apparently different from the case for the **1CuCe-NR** samples, the EXAFS data do not reveal any Cu–Ce contribution in **1CuCe-NP**, in agreement with the HAADF results (Figure S9 in the Supporting Information) that the **1CuCe-NP** sample could contain very small CuO_x clusters. Meanwhile, in situ DRIFTS experiments were carried out to

DOI: 10.1021/acscatal.6b03234
ACS Catal. 2017, 7, 1313–1329

investigate the $Cu^{\delta+}$ species on the catalyst surface. Figure S10 in the Supporting Information shows that, at 2108 cm^{-1}, a strong single band corresponding to the Cu^{+}-CO species is observed. All of the above results confirm that CeO_2-{111}/{100} in both the **NS** and **NP** samples induce strongly synergic effects between copper oxide and ceria, which favor the formation of Cu(I). Therefore, **1CuCe-NP** and **1CuCe-NS** exhibit similar activities in CO oxidation.

3.3.2. Surface Reconstruction of CeO_2—NR under Different Pretreatments. It has been reported that the CeO_2 nanorods calcined at high temperature are enclosed by {111} planes,[25,61] no longer by {110}/{100} planes, which indicates that surface structure reconstruction happened due to the calcination for CeO_2 nanorods. Could such a surface structure reconstruction happen at temperatures below 700 °C? In our system, partial surface reconstruction was found for **CeO_2-NR** calcined at 400 °C (Figure 10b,d and Figure S11b,d in the Supporting Information) in comparison with the untreated **CeO_2-NR** (Figure 10a and Figure S11a). The rectangular cross section of the uncalcined **CeO_2-NR** confirms the exposed surface of {110}/{100}, which is consistent with the previous reports.[11,12] However, a round shape for the cross section suggests that the exposed surface of the calcined **CeO_2-NR** cannot be determined, being closer to mixed planes. The more interesting and important discovery is that the loaded copper oxide on the uncalcined **CeO_2-NR** could inhibit the surface reconstruction of the **1CuCe-NR** catalyst (denoted **1CuCe-NR U-C**) under calcination at 400 °C for 4 h (Figure 10c and Figure S11c).

We further investigated the reactivity of the **1CuCe-NR** catalyst with calcined **CeO_2-NR** as support (denoted **1CuCe-NR C-C**). It is interesting that the **1CuCe-NR C-C** catalyst exhibits obviously enhanced catalytic reactivity in comparison with **1CuCe-NR U-C**, close to that of the **1CuCe-NS C-C** sample (Figure S12a in the Supporting Information). The apparent activation energy value is ca. 54 kJ mol^{-1} for **1CuCe-NR C-C**, which is nearly the same as that of **1CuCe-NR U-C**, indicating that they both follow the same reaction pathway. The H_2-TPR (Figure S12b) and in situ DRIFTS (Figure S13 in the Supporting Information) results for **1CuCe-NR C-C** are obviously different from those of the **1CuCe-NR U-C** sample; however, they are very similar to those of the **1CuCe-NS C-C** sample. On the basis of the above results, we think that the uncalcined **CeO_2-NR** support exposes the intrinsic {110}/{100} plane, while partial surface reconstruction from {110}/{100} to the most stable {111} has occurred in calcined **CeO_2-NR**. In order to get the crystal plane effect of {110}/{100}, we selected the uncalcined **CeO_2-NR** as support, not the **CeO_2-NR** calcined at 400 °C.

3.3.3. Crystal Plane Effect of Ceria in High Cu Loading Catalyst and Other Catalytic Reactions. Regarding the higher Cu loading (5 wt %), no separated Cu-containing phase was generated (Figure S14a in the Supporting Information); meanwhile, the HRTEM and corresponding elemental mapping results (Figure S15 in the Supporting Information) also confirmed that the Cu and Ce elements were homogeneously distributed. Unsurprisingly, the **5CuCe-NS** sample is much more active than **5CuCe-NR** (Figure S14b). Meanwhile, in situ DRIFTS data in Figure S16 in the Supporting Information showed a strong single band corresponding to Cu^{+}-CO (2110 cm^{-1}) for **5CuCe-NS** in comparison to **5CuCe-NR** (2107 cm^{-1}), which is in agreement with the activity. Therefore, similar crystal plane effects also exist in **5CuCe** catalysts, in which the activity is obviously enhanced due to the increase in CuO_x species on the CeO_2 surface.

To assess whether the crystal plane effect of ceria in the CO oxidation activity is in agreement with other similar CO oxidation reactions, such as in CO preferential oxidation (CO-PROX) and water-gas shift (WGS) reactions (Figure S17 in the Supporting Information), a series of experiments were carried out; for either the PROX or the WGS reaction, the CeO_2-{111}/{100} samples always had a obvious positive effect on CO conversion over the whole range in comparison with CeO_2-{110}/{100}. According to previous reports, the partially reduced dispersed copper oxide should be the active site for CO-PROX/WGS reactions.[59,62,63] Therefore, CeO_2-{111}/{100} is crucial for the reduction of CuO, which should result from the stronger synergic interactions between copper and ceria species with CuO_x clusters or similar single CuO_x atom formation.

4. DISCUSSION

CO oxidation as a probe reaction for catalytic mechanisms has been extensively studied. However, this simple reaction, catalyzed by nanocopper catalysts, is still very difficult to understand in depth. It is known that various factors, including the structure of copper species, the oxide support, and the metal—support interaction interdependently influence the catalytic performance. Among them, the metal—support interaction is most complex, which varies with synthetic method, pretreatment conditions, and morphology of the support. In this study, we examined **1CuCe** catalysts with differently faced ceria: the **CeO_2-NR** exposed {110}/{100} faces and **CeO_2-NS** and **-NP** with {111}/{100} faces. In addition to exposing different faces, the existence of different copper oxide species with correspondingly induced reduction abilities probably as a consequence of differences in copper oxide species interacting with diverse CeO_2 faces has also been considered, as shown in Scheme 1, in which the structural evolutions of the **1CuCe** catalysts are displayed. Here, the relation between the structural characteristics and catalytic properties of the **1CuCe** catalysts is further discussed in the following two aspects.

Scheme 1. Schematic Demonstration of the Structural Evolutions of the 1CuCe-NR and 1CuCe-NS Catalysts

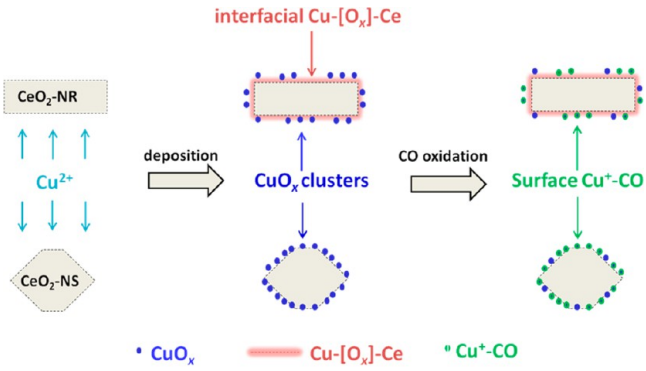

4.1. Interaction between Copper and Ceria in the As-Prepared Catalysts. In the fresh **1CuCe-NS** and **1CuCe-NR** catalysts, the copper oxide is well dispersed on ceria, forming very small clusters (<1 nm) according to Cs-corrected HAADF-STEM. Further characterization of the structure of

DOI: 10.1021/acscatal.6b03234
ACS Catal. 2017, 7, 1313−1329

the **1CuCe-NS** sample has demonstrated that the low-temperature reduction peak centered at 160 °C (α) in the H_2-TPR results (Figure 4) can be attributed to the CuO_x clusters, which is in good agreement with the first shell of the Cu−O structure identified by EXAFS analysis (Figure 3c). However, for the **1CuCe-NR** sample, apart from the low-temperature reduction peak at 190 °C corresponding to CuO_x clusters, a high-temperature peak located at 268 °C (β) originating from the strong interaction of the Cu-[O_x]-Ce structure has been identified (Figure 3d). This is a consequence of the different strengths of the interaction of CuO_x with different types of exposed faces present in the ceria, causing obvious differences in the structures of copper oxide species between **1CuCe-NS** and **1CuCe-NR** (as shown in Scheme 1) that induce a substantial effect on the catalytic reactivity for CO oxidation. Meanwhile, the difference in specific surface areas for **1CuCe-NS** and **1CuCe-NR** catalysts also should be considered; as mentioned above, this area is twice as large for **1CuCe-NS** in comparison to that for the **1CuCe-NR** sample, which may favor a better dispersion of copper oxide on the **CeO_2-NS** surface. Unfortunately the Cu dispersion cannot be determined precisely due to the interference of ceria, which makes it impossible to compare the Cu dispersion in **1CuCe-NS** with that of **1CuCe-NR** sample. However, considering that **1CuCe-NP** also exhibits much higher reactivity in comparison to the **1CuCe-NR** sample and the fact that H_2-TPR, EXAFS, and in situ DRIFTS results are similar to those of **1CuCe-NS**, while they are comparable in surface area (123 m^2 g^{-1} vs 92 m^2 g^{-1}), we can draw a conclusion that the specific surface area does not play a crucial role in catalysis. Thus, it is the differences in interactions between copper and ceria species that cause obvious differences in the dispersion of active copper sites and in the structure of copper oxide species, rather than specific surface area, that induced different reactivities for variously shaped copper−ceria catalysts.

4.2. Reduction of Cu(II) → Cu(I) in the As-Prepared Catalysts. It is well-known that the reactivity of copper−ceria catalysts is related to the synergic effect between copper and ceria. The redox cycles between Cu(II)/Cu(I) and Ce(IV)/Ce(III) are commonly considered to be the key steps in determining the catalytic behavior. Thus, the formation of Cu(I) entities as active sites is an important factor in promoting the activity of CO oxidation. In our work, the copper species were Cu(II) in both the fresh **1CuCe-NS** and **1CuCe-NR** catalysts according to XANES (Figure 3a,b). However, with the aid of in situ DRIFTS (Figures 8 and 9), we found that Cu(I) species were much more easily formed during CO oxidation in **1CuCe-NS** in comparison to the **1CuCe-NR** sample, which is consistent with the previous theoretical simulation results that Cu atoms adsorbed on CeO_2-{111} preferred to be Cu(I),[29] whereas they were Cu(II)[30] on the CeO_2-{110} face. It is noted that the surface of **CuCe-NR** is terminated by {110} and {100} faces, while the **CuCe-NS** or **CuCe-NP** exposes {111} and {100} faces. While in this work we focused more on the comparison between {110} and {111}, the contribution of the {100} face to the structure and catalytic properties should also be discussed. Researchers have prepared cubic-shaped nanocubes (**NC**) with exposing faces of {100}; however, using this CeO_2−NC as support, copper oxides deposited on it were formed as nanoparticles,[64] not sub-nanometer clusters. Such a difference in size of copper oxide makes it difficult to establish comparable catalyst systems using NR, NS, and NC together. Previous results conducted by others on the basis of the near-ambient XPS experiments combining DFT+U calculations have proved that the formation of interfacial Cu(I) species in Cu/CeO_2-NC was not favored due to the higher degree of electron transfer from the interfacial reduced copper oxide toward the CeO_2-{100} face.[65] Therefore, we think that the difference in catalytic reactivity between **CuCe-NS/NP** and **CuCe-NR** comes from the crystal plane effect of {110} vs {111} of ceria, since both **CuCe-NS/NP** and **CuCe-NR** have {100} terminated surfaces. On the basis of our experimental evidence and the above perspective, we can draw the conclusion that the differences in redox properties between **CuCe-NS/NP** and **CuCe-NR** samples as a function of the ceria crystal plane effect seems to be the most important factor that determines the catalytic properties.

5. CONCLUSIONS

In this work, sub-nanometer copper oxide clusters (1 wt % Cu loading) deposited on both ceria nanospheres with {111}/{100} faces and nanorods exposing {110}/{100} faces have been prepared for an investigation of crystal plane effects for CO oxidation. **1CuCe-NS** with exposed CeO_2-{111}/{100} exhibited much higher activity in comparison to **1CuCe-NR** terminated by CeO_2-{110}/{100} faces: the reaction rate values for **1CuCe-NR** and **1CuCe-NS** are 1.8×10^{-6} mol_{co} g_{cat}^{-1} s^{-1} (at 118 °C) and 5.7×10^{-6} mol_{co} g_{cat}^{-1} s^{-1} (at 104 °C), respectively. Full structural investigations revealed that the Cu species in **1CuCe-NR** existed in both Cu-[O_x]-Ce and CuO_x clusters, while the CuO_x clusters exclusively dominated in **1CuCe-NS**. Furthermore, it was found that the strongly bound Cu-[O_x]-Ce structure was adverse to the formation of Cu(I) species, while the CuO_x clusters were easily reduced to Cu(I) species when they were subjected to interaction with CO. The stronger reduction trend of Cu(II) → Cu(I) in **1CuCe-NS** induced by the relatively weak interaction between CuO_x and the CeO_2-{111} face is considered to be the intrinsic reason that ensures the high activity of the **CuCe-NS** catalysts. These results not only give insight into the crystal plane effects of supported catalysts but also favor a comprehensive understanding of the structure−function relation of solid materials at the atomic level.

■ ASSOCIATED CONTENT

Supporting Information

The Supporting Information is available free of charge on the ACS Publications website at DOI: 10.1021/acscatal.6b03234.

TEM/HRTEM/STEM-EDS mapping images of the used **1CuCe-NS** and **1CuCe-NR** catalysts, EXAFS real-part spectra in *R* space of **1CuCe** catalysts before and after CO oxidation reactions, background spectra and hydroxyl species for **1CuCe-NR** and **1CuCe-NS** catalysts under in situ DRIFTS, XRD patterns, H_2-TPR profile, aberration-corrected HAADF-STEM images, XANES/EXAFS, and in situ DRIFTS on the **1CuCe-NP** samples, HRTEM images of the cross-sectional samples for **CeO_2-NR**, **1CuCe-NR U-C**, and **1CuCe-NR C-C** samples, CO conversion and H_2-TPR profile of **1CuCe-NR U-C**, **1CuCe-NR C-C**, and **1CuCe-NS C−C** samples, in situ DRIFTS on the **1CuCe-NR C−C** samples, XRD patterns, TEM/HRTEM images, in situ DRIFTS, and catalytic reactivity for CO oxidation on **5CuCe-NS** and **5CuCe-NR** samples, and a comparison of catalytic reactivity for CO oxidation, WGS, and PROX reactions

DOI: 10.1021/acscatal.6b03234
ACS Catal. 2017, 7, 1313−1329

on **1CuCe-NS**, **1CuCe-NR**, and **1CuCe-NP** samples (PDF)

AUTHOR INFORMATION

Corresponding Authors

*E-mail for R.S.: sirui@sinap.ac.cn.
*E-mail for C.M.: cma@ustc.edu.cn.
*E-mail for C.-J.J.: jiacj@sdu.edu.cn.

ORCID

Chun-Jiang Jia: 0000-0002-4254-5100

Notes

The authors declare no competing financial interest.

ACKNOWLEDGMENTS

Financial support from the National Science Foundation of China (NSFC) (grant nos. 21301107, 21373259, 21331001, and 21501109), the Excellent Young Scientists Funding from the NSFC (grant no. 21622106), the Taishan Scholar Project of Shandong Province of China, and the Hundred Talents Project of the Chinese Academy of Sciences, Doctoral Funding of Shandong Province of China (grant nos. BS2014CL008), Doctoral Funding of Ministry of Education of China (grant nos. 20130131120009), Open Funding from Beijing National Laboratory for Molecular Science, and the Strategic Priority Research Program of the Chinese Academy of Sciences (grant no. XDA09030102) is acknowledged.

REFERENCES

(1) Kim, F.; Connor, S.; Song, H.; Kuykendall, T.; Yang, P. D. *Angew. Chem., Int. Ed.* **2004**, *43*, 3673−3677.
(2) Yang, Y. Y.; Sun, S. G. *J. Phys. Chem. B* **2002**, *106*, 12499−12507.
(3) Xu, Z. N.; Sun, J.; Lin, C. S.; Jiang, X. M.; Chen, Q. S.; Peng, S. Y.; Wang, M. S.; Guo, G. C. *ACS Catal.* **2013**, *3*, 118−122.
(4) Ma, R.; Semagina, N. *J. Phys. Chem. C* **2010**, *114*, 15417−15423.
(5) Bratlie, K. M.; Lee, H.; Komvopoulos, K.; Yang, P. D.; Somorjai, G. A. *Nano Lett.* **2007**, *7*, 3097−3101.
(6) Xie, X. W.; Li, Y.; Liu, Z. Q.; Haruta, M.; Shen, W. J. *Nature* **2009**, *458*, 746−749.
(7) Yang, H. G.; Liu, G.; Qiao, S. Z.; Sun, C. H.; Jin, Y. G.; Smith, S. C.; Zou, J.; Cheng, H. M.; Lu, G. Q. *J. Am. Chem. Soc.* **2009**, *131*, 4078−4083.
(8) Yang, H. G.; Sun, C. H.; Qiao, S. Z.; Zou, J.; Liu, G.; Smith, S. C.; Cheng, H. M.; Lu, G. Q. *Nature* **2008**, *453*, 638−642.
(9) Hua, Q.; Cao, T.; Gu, X. K.; Lu, J. Q.; Jiang, Z. Q.; Pan, X. R.; Luo, L. F.; Li, W. X.; Huang, W. X. *Angew. Chem., Int. Ed.* **2014**, *53*, 4856−4861.
(10) Sun, Y. F.; Liu, Q. H.; Gao, S.; Cheng, H.; Lei, F. C.; Sun, Z. H.; Jiang, Y.; Su, H. B.; Wei, S. Q.; Xie, Y. *Nat. Commun.* **2013**, *4*, 2899.
(11) Zhou, K. B.; Wang, X.; Sun, X. M.; Peng, Q.; Li, Y. D. *J. Catal.* **2005**, *229*, 206−212.
(12) Mai, H. X.; Sun, L. D.; Zhang, Y. W.; Si, R.; Feng, W.; Zhang, H. P.; Liu, H. C.; Yan, C. H. *J. Phys. Chem. B* **2005**, *109*, 24380−24385.
(13) Nolan, M.; Watson, G. W. *J. Phys. Chem. B* **2006**, *110*, 16600−16606.
(14) Huang, M.; Fabris, S. *J. Phys. Chem. C* **2008**, *112*, 8643−8648.
(15) Wu, Z. L.; Li, M. J.; Overbury, S. H. *J. Catal.* **2012**, *285*, 61−73.
(16) Wang, X.; Jiang, Z. Y.; Zheng, B. J.; Xie, Z. X.; Zheng, L. S. *CrystEngComm* **2012**, *14*, 7579−7582.
(17) Huang, X. S.; Sun, H.; Wang, L. C.; Liu, Y. M.; Fan, K. N.; Cao, Y. *Appl. Catal., B* **2009**, *90*, 224−232.
(18) Gao, Y. X.; Wang, W. D.; Chang, S. J.; Huang, W. X. *ChemCatChem* **2013**, *5*, 3610−3620.
(19) Hu, Z.; Liu, X. F.; Meng, D. M.; Guo, Y.; Guo, Y. L.; Lu, G. Z. *ACS Catal.* **2016**, *6*, 2265−2279.
(20) Si, R.; Flytzani-Stephanopoulos, M. *Angew. Chem., Int. Ed.* **2008**, *47*, 2884−2887.
(21) Huang, H.; Dai, Q. G.; Wang, X. Y. *Appl. Catal., B* **2014**, *158−159*, 96−105.
(22) Chang, S. J.; Li, M.; Hua, Q.; Zhang, L. J.; Ma, Y. S.; Ye, B. J.; Huang, W. X. *J. Catal.* **2012**, *293*, 195−204.
(23) Liu, X. W.; Zhou, K. B.; Wang, L.; Wang, B. Y.; Li, Y. D. *J. Am. Chem. Soc.* **2009**, *131*, 3140−3141.
(24) Lee, Y. J.; He, G. H.; Akey, A. J.; Si, R.; Flytzani-Stephanopoulos, M.; Herman, I. P. *J. Am. Chem. Soc.* **2011**, *133*, 12952−12955.
(25) Ta, N.; Liu, J. Y.; Chenna, S.; Crozier, P. A.; Li, Y.; Chen, A.; Shen, W. J. *J. Am. Chem. Soc.* **2012**, *134*, 20585−20588.
(26) Liu, W.; Flytzani-Stephanopoulos, M. *Chem. Eng. Sci.* **1996**, *64*, 283−294.
(27) Gamarra, D.; Camara, A. L.; Monte, M.; Rasmussen, S. B.; Chinchilla, L. E.; Hungria, A. B.; Munuera, G.; Gyorffy, N.; Schay, Z.; Corberan, V. C.; Conesa, J. C.; Martinez-Ariasa, A. *Appl. Catal., B* **2013**, *130-131*, 224−238.
(28) Yao, S. Y.; Mudiyanselage, K.; Xu, W. Q.; Johnston-Peck, A. C.; Hanson, J. C.; Wu, T. P.; Stacchiola, D.; Rodriguez, J. A.; Zhao, H. Y.; Beyer, K. A.; Chapman, K. W.; Chupas, P. J.; Martínez-Arias, A.; Si, R.; Bolin, T. B.; Liu, W. J.; Senanayake, S. D. *ACS Catal.* **2014**, *4*, 1650−1661.
(29) Yang, Z. X.; He, B. L.; Lu, Z. S.; Hermansson, K. *J. Phys. Chem. C* **2010**, *114*, 4486−4494.
(30) Cui, L. X.; Tang, Y. H.; Zhang, H.; Hector, L. G.; Ouyang, C. Y.; Shi, S. Q.; Li, H.; Chen, L. Q. *Phys. Chem. Chem. Phys.* **2012**, *14*, 1923−1933.
(31) Zhou, K. B.; Xu, R.; Sun, X. M.; Chen, H. D.; Tian, Q.; Shen, D. X.; Li, Y. D. *Catal. Lett.* **2005**, *101*, 169−173.
(32) Han, J.; Kim, H. J.; Yoon, S.; Lee, H. *J. Mol. Catal. A: Chem.* **2011**, *335*, 82−88.
(33) Qi, L.; Yu, Q.; Dai, Y.; Tang, C. J.; Liu, L. J.; Zhang, H. L.; Gao, F.; Dong, L.; Chen, Y. *Appl. Catal., B* **2012**, *119−120*, 308−320.
(34) Ma, L.; Wang, D. S.; Li, J. H.; Bai, B. Y.; Fu, L. X.; Li, Y. D. *Appl. Catal., B* **2014**, *148−149*, 36−43.
(35) Wang, W. W.; Du, P. P.; Zou, S. H.; He, H. Y.; Wang, R. X.; Jin, Z.; Shi, S.; Huang, Y. Y.; Si, R.; Song, Q. S.; Jia, C. J.; Yan, C. H. *ACS Catal.* **2015**, *5*, 2088−2099.
(36) Jia, A. P.; Jiang, S. Y.; Lu, J. Q.; Luo, M. F. *J. Phys. Chem. C* **2010**, *114*, 21605−21610.
(37) Yu, H. S.; Wei, X. J.; Li, J.; Gu, S. Q.; Zhang, S.; Wang, L. H.; MA, J. Y.; Li, L. N.; Gao, Q.; Si, R.; Sun, F. F.; Wang, Y.; Song, F.; Xu, H. J.; Yu, X. H.; Zou, Y.; Wang, J. Q.; Jiang, Z.; Huang, Y. Y. *Nucl. Sci. Technol.* **2015**, *26*, 050102.
(38) Wu, Z. L.; Li, M. J.; Howe, J.; Meyer, H. M., III; Overbury, S. H. *Langmuir* **2010**, *26*, 16595−16606.
(39) Deng, W. L.; Frenkel, A. L.; Si, R.; Flytzani-Stephanopoulos, M. *J. Phys. Chem. C* **2008**, *112*, 12834−12840.
(40) Yang, Q.; Fu, X. P.; Jia, C. J.; Ma, C.; Wang, X.; Zeng, J.; Si, R.; Zhang, Y. W.; Yan, C. H. *ACS Catal.* **2016**, *6*, 3072−3082.
(41) Zhao, F. Z.; Chen, S. H.; Zhou, J. L.; Zhang, A. Q. *J. Porous Mater.* **2012**, *19*, 869−876.
(42) Sedmak, G.; Hočevar, S.; Levec, J. *J. Catal.* **2003**, *213*, 135−150.
(43) Moreno, M.; Baronetti, G. T.; Laborde, M. A.; Mariño, F. J. *Int. J. Hydrogen Energy* **2008**, *33*, 3538−3542.
(44) Martínez-Arias, A.; Fernández-García, M.; Soria, J.; Conesa, J. C. *J. Catal.* **1999**, *182*, 367−377.
(45) Liu, W.; Sarofim, A. F.; Flytzani-stephanopoulos, M. *Chem. Eng. Sci.* **1994**, *49*, 4871−4888.
(46) Markaryan, G. L.; Ikryannikova, L. N.; Muravieva, G. P.; Turakulova, A. O.; Kostyuk, B. G.; Lunina, E. V.; Lunin, V. V.; Zhilinskaya, E.; Aboukais, A. *Colloids Surf., A* **1999**, *151*, 435−447.
(47) Bozo, C.; Guilhaume, N.; Herrmann, J. M. *J. Catal.* **2001**, *203*, 393−406.
(48) Zabilskiy, M.; Djinović, P.; Tchernychova, E.; Tkachenko, O. P.; Kustov, L. M.; Pintar, A. *ACS Catal.* **2015**, *5*, 5357−5365.

DOI: 10.1021/acscatal.6b03234
ACS Catal. 2017, 7, 1313−1329

(49) Manzoli, M.; Monte, R. D.; Boccuzzi, F.; Coluccia, S.; Kašpar, J. *Appl. Catal., B* **2005**, *61*, 192−205.
(50) Wan, H. Q.; Wang, Z.; Zhu, J.; Li, X. W.; Liu, B.; Gao, F.; Dong, L.; Chen, Y. *Appl. Catal., B* **2008**, *79*, 254−261.
(51) Tikhov, S. F.; Sadykov, V. A.; Kryukova, G. N.; Paukshtis, E. A.; Popovskii, V. V.; Starostina, T. G.; Kharlamov, G. V.; Anufrienko, V. F.; Poluboyarov, V. F.; Razdobarov, V. A.; Bulgakov, N. N.; Kalinkin, A. V. *J. Catal.* **1992**, *134*, 506−524.
(52) Kydd, R.; Ferri, D.; Hug, P.; Scott, J.; Teoh, W. Y.; Amal, R. *J. Catal.* **2011**, *277*, 64−71.
(53) Gamarra, D.; Martínez-Arias, A. *J. Catal.* **2009**, *263*, 189−195.
(54) Binet, C.; Daturi, M.; Lavalley, J. C. *Catal. Today* **1999**, *50*, 207−225.
(55) Pozdnyakova, O.; Teschner, D.; Wootsch, A.; Kröhnert, J.; Steinhauer, B.; Sauer, H.; Toth, L.; Jentoft, F. C.; Knop-Gericke, A.; Paál, Z.; Schlögl, R. *J. Catal.* **2006**, *237*, 1−16.
(56) Ke, J.; Xiao, J. W.; Zhu, W.; Liu, H. C.; Si, R.; Zhang, Y. W.; Yan, C. H. *J. Am. Chem. Soc.* **2013**, *135*, 15191−15200.
(57) Davó-Quiñonero, A.; Navlani-García, M.; Lozano-Castelló, D.; Bueno-López, A.; Anderson, J. A. *ACS Catal.* **2016**, *6*, 1723−1731.
(58) Gamarra, D.; Munuera, G.; Hungría, A. B.; Fernández-García, M.; Conesa, J. C.; Midgley, P. A.; Wang, X. Q.; Hanson, J. C.; Rodríguez, J. A.; Martínez-Arias, A. *J. Phys. Chem. C* **2007**, *111*, 11026−11038.
(59) Gamarra, D.; Belver, C.; Fernández-García, M.; Martínez-Arias, A. *J. Am. Chem. Soc.* **2007**, *129*, 12064−12065.
(60) Gamarra, D.; Fernández-García, M.; Belver, C.; Martínez-Arias, A. *J. Phys. Chem. C* **2010**, *114*, 18576−18582.
(61) Yang, C. W.; Yu, X. J.; Heiβer, S.; Nefedov, A.; Colussi, S.; Llorca, J.; Trovarelli, A.; Wang, Y. M.; Wöll, C. *Angew. Chem., Int. Ed.* **2017**, *56*, 375−379.
(62) Yao, S. Y.; Xu, W. Q.; Johnston-Peck, A. C.; Zhao, F. Z.; Liu, Z. Y.; Luo, S.; Senanayake, S. D.; Martínez-Arias, A.; Liu, W. J.; Rodriguez, J. A. *Phys. Chem. Chem. Phys.* **2014**, *16*, 17183−17195.
(63) Wang, X. Q.; Rodriguez, J. A.; Hanson, J. C.; Gamarra, D.; Martínez-Arias, A.; Fernández-García, M. *J. Phys. Chem. B* **2006**, *110*, 428−434.
(64) Si, R.; Raitano, J.; Yi, N.; Zhang, L. H.; Chan, S. W.; Flytzani-Stephanopoulos, M. *Catal. Today* **2012**, *180*, 68−80.
(65) Monte, M.; Munuera, G.; Costa, D.; Conesa, J. C.; Martínez-Arias, A. *Phys. Chem. Chem. Phys.* **2015**, *17*, 29995−30004.

DOI: 10.1021/acscatal.6b03234
ACS Catal. 2017, 7, 1313−1329